Testing eccentric corrections to the radiation-reaction force in the test-mass limit of effective-one-body models

Guglielmo Faggioli,[1, *] Maarten van de Meent,[2, 1] Alessandra Buonanno,[1, 3]
Aldo Gamboa,[1] Mohammed Khalil,[4] and Gaurav Khanna[5, 6, 7]

[1] Max Planck Institute for Gravitational Physics (Albert Einstein Institute), Am Mühlenberg 1, Potsdam 14476, Germany
[2] Niels Bohr International Academy, Niels Bohr Institute, Blegdamsvej 17, 2100 Copenhagen, Denmark
[3] Department of Physics, University of Maryland, College Park, MD 20742, USA
[4] Perimeter Institute for Theoretical Physics, 31 Caroline Street North, Waterloo, ON N2L 2Y5, Canada
[5] Department of Physics and Center for Computational Research, University of Rhode Island, Kingston, RI 02881, USA
[6] Department of Physics, University of Massachusetts, Dartmouth, MA 02747, USA
[7] Center for Scientific Computing and Data Science Research, University of Massachusetts, Dartmouth, MA 02747, USA

In this work, we test an effective-one-body radiation-reaction force for eccentric planar orbits of a test mass in a Kerr background, which contains third-order post-Newtonian (PN) non-spinning and second-order PN spin contributions. We compare the analytical fluxes connected to two different resummations of this force, truncated at different PN orders in the eccentric sector, with the numerical fluxes computed through the use of frequency- and time-domain Teukolsky-equation codes. We find that the different PN truncations of the radiation-reaction force show the expected scaling in the weak gravitational-field regime, and we observe a fractional difference with the numerical fluxes that is $< 5\%$, for orbits characterized by eccentricity $0 \leq e \leq 0.7$, central–black-hole spin $-0.99M \leq a \leq 0.99M$ and fixed orbital-averaged quantity $x = \langle M\Omega \rangle^{2/3} = 0.06$, corresponding to the mildly strong-field regime with semilatera recta $9M < p < 17M$. Our analysis provides useful information for the development of spin-aligned eccentric models in the comparable-mass case.

I. INTRODUCTION

The observation of gravitational waves (GWs) with the LIGO-Virgo [1–3] and LIGO-Virgo-KAGRA (LVK) [4] collaborations marked a new era in gravitational physics, uncovering unique properties of stellar-mass black holes (BHs) and neutron stars. As future data acquisition becomes characterized by increased sensitivity, it is necessary to improve the precision and accuracy of waveform models used for matched-filtering and parameter-estimation pipelines. In particular, modeling waveforms from eccentric and precessing-spin binaries will become increasingly important. This is further motivated by the fact that upcoming observational runs [5] and future detectors, like the Einstein Telescope [6], Cosmic Explorer [7] and LISA [8], will increase the number of detections by a factor $\sim 10^3$ and be able to probe binary's subpopulations, in lower frequency bands and for smaller mass ratios, which can exhibit larger eccentricities [9–12].

While eccentricity decreases toward merger due to the energy and angular momentum loss caused by the emission of GWs [13, 14], the residual eccentricity can help constrain different binary-formation scenarios and thus the origin of GW sources [15–18]. Indeed, the eccentricity is indicative of binaries formed through dynamical formation channels, which could occur in dense stellar environments, like globular clusters, where the three-body Kozai-Lidov mechanism [19, 20] or dynamic capture [18, 21–24] play a role. Efforts are currently underway to detect signs of orbital eccentricity in the GW signals observed by the LVK detectors [25–35].

Among the different methods to solve the two-body problem in general relativity, the effective-one-body (EOB) approach [36, 37] is a framework that provides accurate and fast waveforms for quasi-circular (QC) binaries [38–49], due to a strong synergy between analytical approximation methods and numerical relativity (NR) results.

In recent years, generalizations of EOB models to eccentric inspirals have been developed [50–61]. In particular, Ref. [60] derived the second-order post-Newtonian (PN) expressions for the radiation-reaction (RR) force and gravitational-waveform modes for eccentric inspirals. They include tail effects, in addition to spin-orbit (SO) and spin-spin (SS) couplings. Reference [61] introduced the `SEOBNRv4EHM` model: an extension of the QC `SEOBNRv4HM` model [44] to eccentric orbits, where the authors showed an EOB/NR unfaithfulness less than 1% when comparing with the 28 eccentric NR simulations that were publicly available at the time from the Simulating eXtreme Spacetimes (SXS) collaboration [62, 63]. However, in the work of Ref. [61], the dynamics of the binary is modeled through the use of the QC RR force from the `SEOBNRv4HM` model, and the eccentric corrections are considered only when computing the eccentric waveforms modes introduced in Ref. [60]. By contrast, the more recent waveform model `SEOBNRv5EHM` employs a RR force with eccentric corrections [64].

Among the other examples of eccentric EOB models, we mention `TEOBResumS` [48, 65], which has been extended to eccentric orbits, after investigating several prescriptions for incorporating eccentricity effects, in Refs. [56–59, 66–72]. The latest version of their model,

known as `TEOBResumS-Dalì`, includes eccentric 2PN information, and is characterized by factorizing the leading PN order of the waveform modes and azimuthal component of the RR force, which include high-order time derivatives of the radial separation and orbital frequency. The eccentric 2PN radial component of the RR force is adapted from Ref. [50] and is Padé resummed. The model shows unfaithfulness $\lesssim 1\%$ when compared with the 28 SXS publicly-available eccentric NR waveforms, making its accuracy comparable to the `SEOBNRv4EHM` model.

Several studies [38, 58, 67, 70, 73–77] showed the importance of augmenting EOB waveform models for the plunge-merger and ringdown with insights from BH-perturbation theory. The common approach is to consider a test mass (TM) orbiting or scattering off a Kerr BH and use this system as a laboratory to test and provide benchmarks to the models in the comparable-mass case. Among these works, Refs. [58, 67] assessed different EOB eccentric RR force prescriptions. In particular, Ref. [67] also provides an analysis for a proxy to the `SEOBNRv4HM` QC RR force and of a resummed version of the 2PN eccentric RR force introduced in Ref. [60]. (We will discuss some comparisons with their results in Sec. III A.)

Here, we aim to extend past analyses in different ways. We consider the TM limit of a 3PN-eccentric RR force, recently computed by some of the authors of this work, and which will appear in a forthcoming work [64]. This force is computed employing the same procedure of Ref. [60], but it considers a different gauge choice for the leading-order of the RR force, which avoids a 2.5PN modification (relative to the leading-order) of the QC orbital phase when transforming between harmonic and EOB coordinates. The force that we consider contains the full non-spinning contributions up to 3PN order, and spin contributions only up to 2PN order. For the spin contributions, we employ the 1.5PN spin-orbit (SO) and 2PN spin-spin (SS) parts to the RR force as in Ref. [60], but taking into account the leading-order gauge choice of Ref. [64]. We resum the RR force in two ways: by extracting the QC RR force of `SEOBNRv5HM` [49] as a multiplicative and an additive term. In the TM limit, we remark that this QC RR force differs from the `SEOBNRv4HM` one by new higher-order PN contributions in the waveform modes used for the flux computation, as explained in Ref. [49]. We study the effects of the individual PN eccentric contributions to the RR force in different gravitational-field regimes of the parameter space. The analysis is performed by comparing the analytical fluxes, computed from the eccentric RR force in the TM limit, against numerical fluxes that are computed by solving the Teukolsky equation [79] through the use of a frequency-domain (FD) [80] and a time-domain (TD) [81–83] code. Both fluxes are computed on equatorial geodesics of the Kerr metric. By comparing the fluxes, we test the two resummations of the eccentric RR force, as we explain in detail in Sec. II. In our study, we focus on equatorial bound orbits of Kerr in the weak and

strong gravitational-field regimes, and also explore the RR force for hyperbolic encounters, by comparing the fluxes for some Schwarzschild hyperbolic geodesics with fixed energy.

The article is structured as follows. In Sec. II, we introduce the methodology of our analysis. In particular, Sec. II A describes the EOB model we use in the TM limit and how we compute eccentric-planar geodesics in the Kerr metric. In Sec. II B, we describe how to compute the numerical fluxes by solving the Teukolsky equation numerically, while Sec. II C shows how the analytical fluxes are computed from the RR force through the use of the balance equations. In Sec. III, we provide the main results of our analysis. In particular, Sec. III A gives an overview of the fluxes comparison, and Secs. III B, III C show the results for bound orbits in the Schwarzschild and Kerr spacetime, respectively. Section III D focuses on hyperbolic encounters in Schwarzschild spacetime. Finally, Sec. IV summarizes the results, and points out future steps. In the appendices, we provide supplemental information. Notably, in Appendix A we summarize how the non-spinning 3PN terms of the eccentric RR force are derived and we provide the full TM expressions of the eccentric corrections to the QC RR force, together with the expressions of the Schott terms, which are necessary to compute the instantaneous fluxes. Appendix B provides details on how the instantaneous fluxes are computed from the FD Teukolsky-equation code.

Notations

We adopt natural units $G = c = 1$ and consider a non-spinning TM of mass $\mu = \nu M$ orbiting a Kerr BH of mass M with dimensionless spin $a = J/M^2$. The Kerr metric is expressed in Boyer-Lindquist coordinates $\{T, R, \theta, \varphi\}$ and we restrict our analysis to the equatorial plane, $\theta = \pi/2$. The dynamics of the TM is described by canonical coordinates $\{R, \varphi, P_R, P_\varphi\}$. Throughout this article, we consider scaled dimensionless variables

$$t = \frac{T}{M}, \quad r = \frac{R}{M}, \quad p_r = \frac{P_R}{\mu}, \quad p_\varphi = \frac{P_\varphi}{M\mu}. \quad (1)$$

The Hamiltonian H, and RR force $\mathcal{F} = (\mathcal{F}_r, \mathcal{F}_\varphi)$ are scaled by the TM μ.

II. METHODOLOGY

In this work, we assess the analytical EOB eccentric RR force of Ref. [60], extended to 3PN in the non-spinning part in Ref. [64], by comparing it with numerical results. In particular, as we explain in Sec. II C, we compare numerical fluxes obtained by solving the Teukolsky equation against the analytical fluxes that are connected to the RR force through the energy and angular-momentum balance equations. These fluxes are computed on Kerr equatorial geodesics of a TM. In the fol-

lowing two sections, we describe how the orbits are computed and the methodology used to derive the numerical and analytical fluxes.

A. EOB model in the TM limit

To describe the dynamics of a TM orbiting a Kerr BH in the equatorial plane, we work within the EOB framework [36, 37] and consider the Kerr Hamiltonian restricted to equatorial orbits ($\theta = \pi/2$, $p_\theta = 0$):

$$H = \Lambda^{-1} \left(2ap_\varphi + \sqrt{\Delta p_\varphi^2 r^2 + \Delta^2 \Lambda \frac{p_r^2}{r} + \Delta \Lambda r} \right) , \quad (2)$$

with quantities Λ and Δ being

$$\Lambda = r^3 + 2a^2 + a^2 r , \quad (3a)$$
$$\Delta = a^2 - 2r + r^2 . \quad (3b)$$

Instead of the radial momentum p_r we consider p_{r_*}, which is the momentum conjugate to the tortoise radial coordinate r_*. The tortoise coordinate is related to the Boyer-Lindquist coordinate r by:

$$dr_* = \frac{r^2 + a^2}{\Delta} dr = \frac{1}{\xi(r)} dr , \quad (4a)$$
$$p_{r_*} = \xi(r) p_r . \quad (4b)$$

This is a general practice that is done to improve the numerical stability of the dynamical evolution [74, 84], since p_r diverges at the horizon while p_{r_*} does not. The evolution of the dynamics is provided by the Hamilton equations:

$$\dot{r} = \xi \frac{\partial H}{\partial p_{r_*}}(r, p_{r_*}, p_\varphi) , \quad (5a)$$
$$\dot{\varphi} = \Omega = \frac{\partial H}{\partial p_\varphi}(r, p_{r_*}, p_\varphi) , \quad (5b)$$
$$\dot{p}_{r_*} = -\xi \frac{\partial H}{\partial r}(r, p_{r_*}, p_\varphi) + \mathcal{F}_r , \quad (5c)$$
$$\dot{p}_\varphi = \mathcal{F}_\varphi , \quad (5d)$$

where the dot symbol represents a total derivative with respect to the scaled coordinate time in Eq. (1), Ω is the orbital frequency, scaled by the total mass, and $\mathcal{F} = (\mathcal{F}_r, \mathcal{F}_\varphi)$ corresponds to the RR force connected to the emission of GWs for generic equatorial orbits.

The RR force components we consider, $\mathcal{F}_r$ and $\mathcal{F}_\varphi$, are two resummed versions of the RR force originally computed in Ref. [60] and here extended to 3PN order in the non-spinning eccentric sector [64]. These two resummations are given by:

$$\mathcal{F}_r^{\mathrm{mult}} = \mathcal{F}_r^{\mathrm{QC}} \mathcal{F}_r^{\mathrm{ecc,mult}} , \quad \mathcal{F}_\varphi^{\mathrm{mult}} = \mathcal{F}_\varphi^{\mathrm{QC}} \mathcal{F}_\varphi^{\mathrm{ecc,mult}} \quad (6a)$$
$$\mathcal{F}_r^{\mathrm{add}} = \mathcal{F}_r^{\mathrm{QC}} + \mathcal{F}_r^{\mathrm{ecc,add}} , \quad \mathcal{F}_\varphi^{\mathrm{add}} = \mathcal{F}_\varphi^{\mathrm{QC}} + \mathcal{F}_\varphi^{\mathrm{ecc,add}} , \quad (6b)$$

where $\mathcal{F}_r^{\mathrm{QC}}$ and $\mathcal{F}_\varphi^{\mathrm{QC}}$ are the radial and azimuthal components of the RR force using the QC prescription, while $\mathcal{F}_{r,\varphi}^{\mathrm{ecc,mult}}$ and $\mathcal{F}_{r,\varphi}^{\mathrm{ecc,add}}$ are the eccentric corrections. We refer to the two resummations as the *multiplicative* implementation, given in Eq. (6a) and the *additive* implementation, given in Eq. (6b). The complete expressions in the TM limit of the eccentric corrections are in Appendix A.

The QC RR force $\mathcal{F}^{\mathrm{QC}} = (\mathcal{F}_r^{\mathrm{QC}}, \mathcal{F}_\varphi^{\mathrm{QC}})$ is calculated using the prescription and PN information of the SEOBNRv5HM waveform model [49], defined by the expressions

$$\mathcal{F}_\varphi^{\mathrm{QC}} = -\frac{\Omega}{8\pi} \sum_{\ell=2}^{8} \sum_{m=1}^{\ell} m^2 |d_{\mathrm{L}} h_{\ell m}^{\mathrm{F}}|^2 , \quad (7a)$$
$$\mathcal{F}_r^{\mathrm{QC}} = \frac{p_{r_*}}{p_\varphi} \mathcal{F}_\varphi^{\mathrm{QC}} , \quad (7b)$$

where d_{L} is the luminosity distance of the binary to the observer and $h_{\ell m}^{\mathrm{F}}$ are the GW modes in factorized form [38, 39, 74, 85], given by:

$$h_{\ell m}^{\mathrm{F}} = h_{\ell m}^{(\mathrm{N},\epsilon)} \hat{S}_{\mathrm{eff}}^{(\epsilon)} T_{\ell m} f_{\ell m} e^{i\delta_{\ell m}} . \quad (8)$$

Here, ϵ is the parity of the multipolar waveform mode, such that $\epsilon = 0$ for even $\ell + m$, and $\epsilon = 1$ for odd $\ell + m$. The leading term in Eq. (8), $h_{\ell m}^{(\mathrm{N},\epsilon)}$ is the Newtonian contribution

$$h_{\ell m}^{(\mathrm{N},\epsilon)} = \frac{\nu}{d_L} n_{\ell m}^{(\epsilon)} c_{\ell+\epsilon}(\nu) v_\Omega^\ell Y^{\ell-\epsilon,-m} \left(\frac{\pi}{2}, \phi \right) , \quad (9)$$

where $Y^{\ell-\epsilon,-m}(\theta, \phi)$ are the scalar spherical harmonics, $n_{\ell m}^{(\epsilon)}$ and $c_{\ell+\epsilon}(\nu)$ are functions given in Eqs. (28) and (29) of Ref. [49], and v_Ω is given by

$$v_\Omega = \Omega^{1/3}. \quad (10)$$

Note that the SEOBNRv5HM model uses v_φ instead of v_Ω in Eq. (9), which is given in the TM limit by $v_\varphi = \Omega r_\Omega = \Omega[r^{3/2} + a]^{2/3}$. However, in this work, we use v_Ω since, while computing the eccentric 3PN RR force in Eqs. (5c)-(5d), we realized that the v_φ prescription does not admit a straightforward generalization for eccentric orbits. More details on this choice can be found in Ref. [64].

The function $\hat{S}_{\mathrm{eff}}^{(\epsilon)}$ is the effective source term which is given by

$$\hat{S}_{\mathrm{eff}}^{(\epsilon)} = \begin{cases} H(r, p_{r_*}, p_\varphi), & \epsilon = 0 \\ p_\varphi v_\Omega, & \epsilon = 1 . \end{cases} \quad (11)$$

The factor $T_{\ell m}$ resums the leading order logarithms of tail effects and corresponds to

$$T_{\ell m} = \frac{\Gamma(\ell + 1 - 2i\hat{k})}{\Gamma(\ell + 1)} e^{\pi \hat{k}} e^{2i\hat{k} \ln 2m\Omega r_0} , \quad (12)$$

where Γ is the Euler gamma function, $\hat{k} = m\Omega$ in the TM limit and $r_0 = 2/\sqrt{e}$. The remaining part of the factorized modes (8) is expressed as an amplitude $f_{\ell m}$ and a

phase $\delta_{\ell m}$, which are computed such that the expansion of $h_{\ell m}$ agrees with the PN expanded modes. We point the reader to Appendix B of Ref. [49] for the explicit expressions of the different $f_{\ell m}$ and $\delta_{\ell m}$ terms.

The TM limit of Eqs. (7) and (8) is obtained by setting the mass ratio ν to zero in the expressions, except for the leading ν in the Newtonian prefactor (9).

In our analysis, we consider equatorial planar geodesics of the Kerr background; hence, we consider $\mathcal{F}_r = \mathcal{F}_\varphi = 0$ in Eqs. (5c) and (5d), when evolving the dynamics. We characterize the planar orbits through the parameters $\{p, e, a\}$, which correspond to the semilatus rectum, the eccentricity and the spin of the Kerr BH, respectively. We adopt the *Keplerian parametrization*, where for the definitions of p and e we have:

$$p = \frac{2 r_{\mathrm{a}} r_{\mathrm{p}}}{r_{\mathrm{a}} + r_{\mathrm{p}}} \quad , \quad e = \frac{r_{\mathrm{a}} - r_{\mathrm{p}}}{r_{\mathrm{p}} + r_{\mathrm{a}}} \quad , \tag{13}$$

where r_{a} and r_{p} are the radial separation at the apocenter and at the pericenter, respectively.

As we show in Sec. II C, after evolving Eqs. (5) without RR forces (i.e., for geodesics), we compute the analytical fluxes by evaluating the RR force in Eqs. (6) on the geodesics. Hence, to avoid any possible confusion to the reader we stress that whenever the QC expressions in Eqs. (7) and (8) are employed, they are evaluated on the geodesic although they are quantities constructed assuming QC trajectories.

B. Numerical fluxes

The core of our analysis relies on the computation of the energy flux Φ_E and angular-momentum flux Φ_J radiated by the TM to future null infinity. These fluxes are computed numerically by solving the Teukolsky master equation [79], which in Boyer-Lindquist coordinates reads

$$
\begin{aligned}
&- \left[\frac{(r^2 + a^2)^2}{\Delta} - a^2 \sin^2\theta \right] \partial_{tt}\Psi - \frac{4 a r}{\Delta} \partial_{t\varphi}\Psi \\
&- 2s \left[r - \frac{(r^2 - a^2)}{\Delta} + i a \cos\theta \right] \partial_t\Psi + \Delta^{-s}\partial_r(\Delta^{s+1}\partial_r\Psi) \\
&+ \frac{1}{\sin\theta}\partial_\theta(\sin\theta\,\partial_\theta\Psi) + \left[\frac{1}{\sin\theta^2} - \frac{a^2}{\Delta} \right] \partial_{\varphi\varphi}\Psi \\
&+ 2s \left[\frac{a(r-1)}{\Delta} + \frac{i\cos\theta}{\sin\theta^2} \right] \partial_\varphi\Psi - (s^2 \cot\theta^2 - s)\Psi \\
&= -4\pi(r^2 + a^2\cos\theta^2)\mathcal{T} .
\end{aligned}
\tag{14}
$$

This equation describes the evolution of scalar, vector, and tensor perturbations of a Kerr BH. The function Δ, the spin parameter a and the coordinates correspond to the same quantities defined in the previous sections. The parameter s is the *spin weight* of the field. In particular, when $s = \pm 2$ the equation describes degrees of freedom of gravity that radiate, and for $s = -2$ it is $\Psi = (r -$

$i a \cos\theta)^4 \psi_4$, where ψ_4 is the Weyl curvature scalar that describes outgoing GWs.

A system composed of a TM orbiting a Kerr BH can be interpreted as a perturbed Kerr metric, and within this interpretation the source term $\mathcal{T}$ in the right-hand side of Eq. (14) describes a TM moving in the Kerr spacetime. The details on how the source term $\mathcal{T}$ of the TM is constructed and how Eq. (14) is numerically solved are beyond the scope of this section. We mention the fact that the source term $\mathcal{T}$ of a TM orbiting a Kerr BH is constructed from Dirac-delta functions of the variables r and θ, as well as first and second derivatives of the delta functions in these variables. These terms are sourced at the location of the TM, hence the source $\mathcal{T}$ depends on the trajectory that the TM follows in the Kerr spacetime. The details can be found in Refs. [80, 82, 83]. In this analysis, the trajectories used to source the term $\mathcal{T}$ are the geodesics introduced at the end of Sec. II A, constructed evolving Eqs. (5).

To solve Eq. (14), we make use of two different codes: when considering bound orbits we adopt the FD code of Ref. [80], while when considering unbound orbits we employ the TD code developed in Ref. [81–83]. At future null infinity, the Weyl scalar ψ_4 and the waveform strain $h = h_+ - i h_\times$ are related by the expression

$$\psi_4 = \frac{1}{2}\frac{\partial^2 h}{\partial t^2} = \frac{1}{2}\left(\frac{\partial^2 h_+}{\partial t^2} - i \frac{\partial^2 h_\times}{\partial t^2} \right) , \tag{15}$$

and following standard practices, the waveform is decomposed in spin-weighted spherical harmonics

$$h = \sum_{\ell,m} {}_{-2}Y_{\ell m}(\theta, \varphi)\, h_{\ell m} . \tag{16}$$

The fluxes Φ_E and Φ_J are computed from the modes through the expressions

$$\Phi_E = \frac{1}{16\pi} \sum_{\ell m} |\dot{h}_{\ell m}|^2 , \tag{17a}$$

$$\Phi_J = \frac{1}{16\pi} \sum_{\ell m} m \Im(\dot{h}_{\ell m} h_{\ell m}^*) . \tag{17b}$$

In Appendix B, we give closed form expressions for constructing the instantaneous fluxes from FD Teukolsky solutions. In this work, we truncate the summation over the modes at $\ell = 8$. More details on the numerical errors of the FD and TD Teukolsky codes employed in our analysis can be found in Refs. [75, 80–83].

C. Analytical fluxes

In order to assess the EOB eccentric RR force of Eqs. (6) by comparing with numerical results, it is necessary to compute the analytical fluxes. The connection between the RR force and the fluxes is given by the *balance equations*

$$\dot{E}_{\mathrm{system}} + \Phi_E + \dot{E}_{\mathrm{Schott}} = 0 , \tag{18a}$$

$$\dot{J}_{\text{system}} + \Phi_J + \dot{J}_{\text{Schott}} = 0 \ . \qquad (18b)$$

These equations relate the time-dependent fluxes at future null infinity, Φ_E and Φ_J, to the change in the energy and angular momentum of the system, $\dot{E}_{\text{system}}$ and $\dot{J}_{\text{system}}$, together with two other terms that appear as total time derivatives, $\dot{E}_{\text{Schott}}$ and $\dot{J}_{\text{Schott}}$, known as Schott terms. These two terms take into account the contributions to the fluxes due to the interaction of the system with the radiation field, as originally pointed out in the context of electromagnetism in Ref. [86] and they were introduced in the context of the EOB framework in Ref. [50].

The connection between the fluxes $\Phi_{E/J}$, the RR force $\mathcal{F}$ and the Schott terms is made explicit by first considering the Hamilton equations (5), which lead to

$$\dot{E}_{\text{system}} = \frac{dH}{dt} = \dot{r}\mathcal{F}_r + \dot{\varphi}\mathcal{F}_\varphi \ , \qquad (19a)$$

$$\dot{J}_{\text{system}} = \dot{p}_\varphi = \mathcal{F}_\varphi \ , \qquad (19b)$$

where the fact that the Hamiltonian in Eq. (2) does not depend on the azimuthal angle φ is exploited. By plugging these expressions in Eqs. (18), one gets:

$$\Phi_E = -\dot{r}\mathcal{F}_r - \dot{\varphi}\mathcal{F}_\varphi - \dot{E}_{\text{Schott}} \ , \qquad (20a)$$

$$\Phi_J = -\mathcal{F}_\varphi - \dot{J}_{\text{Schott}} \ . \qquad (20b)$$

From these equations we are able to compute the fluxes from the RR force in Eqs. (6), providing a way to test its prescriptions. This is done by first computing Kerr geodesics as explained in Sec. II A and then evaluating all the quantities involved in the right-hand side of Eqs. (20) on the geodesics. We point the reader to Appendix A for the expressions of the PN time derivatives of the Schott terms, $\dot{E}_{\text{Schott}}$ and $\dot{J}_{\text{Schott}}$, as functions of the EOB dynamical variables, as used in this work.

Note that in the above, we have not included any effects due to the central Kerr BH absorbing GWs, changing its mass and spin. If included, these effects would alter the relationship between the RR forces $\mathcal{F}_{r/\varphi}$ and fluxes $\Phi_{E/J}$ in Eqs. (20). In practice, the effects of absorption are typically several orders of magnitude smaller than the fluxes to infinity see e.g. [87] (but can become order 10% for extreme orbits close to the horizon of a nearly extremal BH [76, 88, 89]). As such, the absorption fluxes are mostly relevant when their effects can accumulate over a large number of orbits in an inspiral. For the single orbit comparisons in this work, their impact would be minimal. Nonetheless, to ensure an apples-to-apples comparison, we also include only the fluxes to infinity in the numerical Teukolsky fluxes.

III. COMPARISON OF THE ANALYTICAL AND NUMERICAL FLUXES

In the following, we present the comparison between the analytical and numerical fluxes computed as ex-

plained in Sec. II. In particular, we focus on studying the different PN contributions in the eccentric part of the analytical fluxes. Throughout this section, we label the fluxes that include PN corrections due to eccentricity at 1PN, 2PN and 3PN order (including SO and SS corrections up to 2PN order), as "ECC1PN", "ECC2PN" and "ECC3PN", while the fluxes that simply use the QC prescription of the fluxes evaluated on an eccentric trajectory are labeled "QC". Note that the fluxes labeled "ECCnPN" still contain all available PN orders in the QC part of the flux.

A. Instantaneous fluxes

We start by comparing the numerical and analytical instantaneous fluxes. Before doing so, we emphasize that the Schott terms in Eqs. (20), are known only as PN expansions up to 3PN order, while the RR force terms have been resummed in the EOB formalism. Consequently, there is a limit to what can be learned when comparing the instantaneous fluxes to the numerical-Teukolsky fluxes in the strong-field regime, as it is unclear whether any particular disagreement is due to an inaccuracy of the RR forces or a breakdown of the PN approximation in the Schott terms. This ambiguity is not present when considering orbit-averaged fluxes, as we mention in Sec. III B. Nonetheless, we believe it is instructive to look at the comparison of the instantaneous fluxes as this helps build an intuitive picture of our analysis.

The comparison of the numerical and analytical fluxes is illustrated in Fig. 1. We consider an orbit with semi-latus rectum $p = 13$, eccentricity $e = 0.5$ and spin $a = 0$. The analytical and numerical fluxes are plotted over a radial period on the bound geodesic. In the left panel, the orbit is shown, while in the top panels the instantaneous fluxes between two consecutive apocenters are plotted. The black curves correspond to the numerical fluxes obtained from the FD Teukolsky code, while the colored lines are the analytical fluxes. We show the QC fluxes (blue curves), which are computed with the QC RR force in Eqs. (7), and the eccentric fluxes ECC1PN (red curves), ECC2PN (orange curves) and ECC3PN (green curves). Finally, the bottom panels of Fig. 1 show the fractional difference between the analytic and Teukolsky fluxes. The analytical fluxes are computed considering the multiplicative implementation (6a). The additive corrections provide similar results to Fig. 1, and are not shown here.

For the geodesic considered in Fig. 1, we do not find a clear improvement of the fluxes at different PN orders along the orbit. Around the apocenter passage (for $t \approx 600$ and $t \approx 1100$ where $r \approx 25$) we observe that the ECC1PN fluxes better approximate the numerical ones, whereas the ECC2PN and ECC3PN fluxes are close, but do not improve the approximation. By removing the eccentric PN tail terms, we find that the 1.5PN tail contribution is degrading the accuracy of the instan-
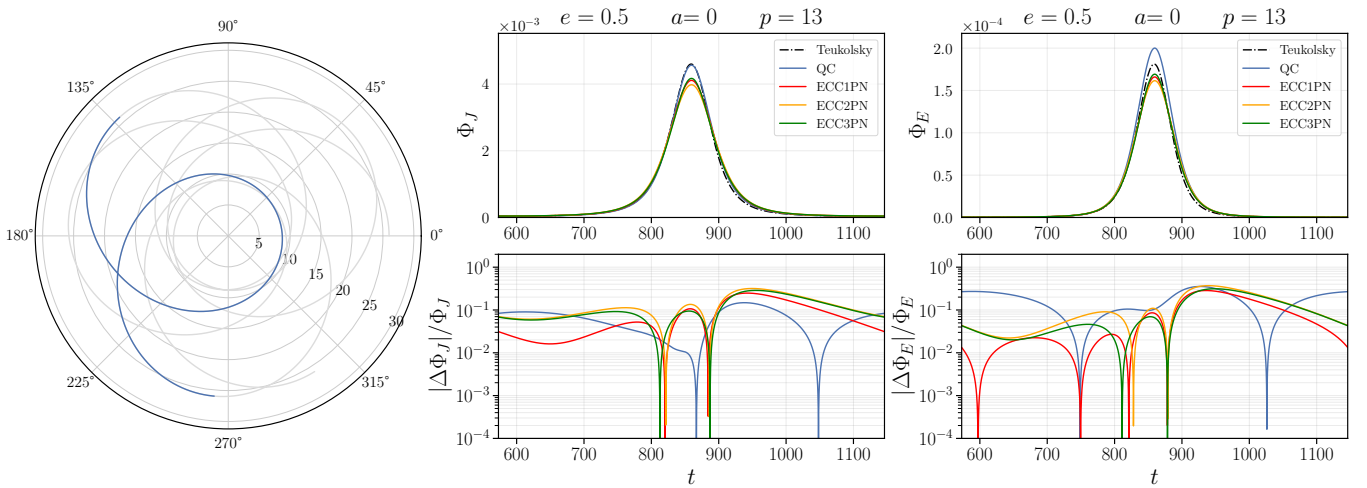
FIG. 1. Fluxes for an eccentric geodesic with $p = 13$, $e = 0.5$ and $a = 0$. On the left panel, the planar orbit is shown, highlighting in blue the trajectory over one radial period. The top panels show the angular momentum Φ_J and energy Φ_E fluxes at infinity: black curves are the Teukolsky fluxes, while colored curves are the analytical fluxes. "QC" refer to the QC fluxes while "ECCnPN" refer to fluxes computed considering eccentric corrections at nPN order. The bottom panels show the relative difference with respect to the Teukolsky fluxes.

taneous results. However, in Sec. III B, we will discuss that these terms are essential to recover the correct scaling in the weak-gravitational field regime when considering the orbit-averaged fluxes. This confirms what we anticipated at the beginning of this section: one PN order may be worse for the instantaneous fluxes, but better for the averaged fluxes, and thus, we cannot conclude from those results if the RR force is accurate since we cannot disentangle it from the effect of the PN-expanded Schott terms.

Near the pericenter passage (for $t \approx 850$ where $r \approx 9$) we find that the ECC3PN energy flux improves the other PN orders, while for the angular-momentum flux it is the QC curve that best approximates the numerical flux. This close agreement of the QC fluxes near the pericenter passage was already pointed out in Ref. [67] for some orbital configurations, and explained as a numerical coincidence. This will become more apparent in Sec. III B, as we show the behavior of this agreement as a function of the orbital separation.

The bottom panels of Fig. 1 show an asymmetry of the relative differences with respect to the pericenter passage. After convincing ourselves that this behavior is not due to any numerical artifact, we find that it comes from an asymmetry of the Teukolsky fluxes with respect to the pericenter. We conclude that this asymmetry arises from contributions that are not modeled by the EOB fluxes, but that are present in the numerical fluxes. By inspecting different orbits and observing the same pattern, especially for orbits that lay in the weak-field regime, we suggest that this asymmetry comes from delayed contributions coming from higher-order-PN tail terms that are not present in the analytical fluxes.

We notice that there are qualitative differences be-

tween our results and Fig. 1 of Ref. [67], despite the two figures ostensibly plotting the same quantities for the same orbit with both the QC and ECC2PN (labeled "QC2PN" in Ref. [67]) much closer to the numerical values in our version. The discrepancy between the QC flux may arise due to the proxy for the QC flux used in Ref. [67] not faithfully reproducing the QC flux of SEOBNRv4HM (and notably the QC flux of SEOBNRv5HM, which is used in this paper). The discrepancy between the ECC2PN fluxes, on the other hand, is due to the fact that in Ref. [67], the authors use the Schott terms of Ref. [50] when computing the fluxes through Eqs. (20). However, this is not compatible with the gauge of the eccentric RR force of Ref. [60], which is used to compute the ECC2PN (QC2PN) fluxes. There is no freedom in using Schott terms in a different gauge, and the ones of Ref. [60] must be considered when computing the instantaneous ECC2PN fluxes.

B. Averaged fluxes: bound orbits in Schwarzschild

Figure 1 indicated that the 1PN eccentric corrections of the multiplicative implementation of the RR force (6a) better approximate the numerical flux than the higher order eccentric PN corrections near the pericenter of the orbit. The additive implementation (6b) (not plotted in Fig. 1) shows similar behavior. This motivates a further investigation, because, in principle, one would expect the higher order PN corrections to improve the approximation, at least in the weak-field regime.

To better assess this, we start by restricting to the Schwarzschild case and we analyze what happens when considering the eccentric force in the weak-field scenario.
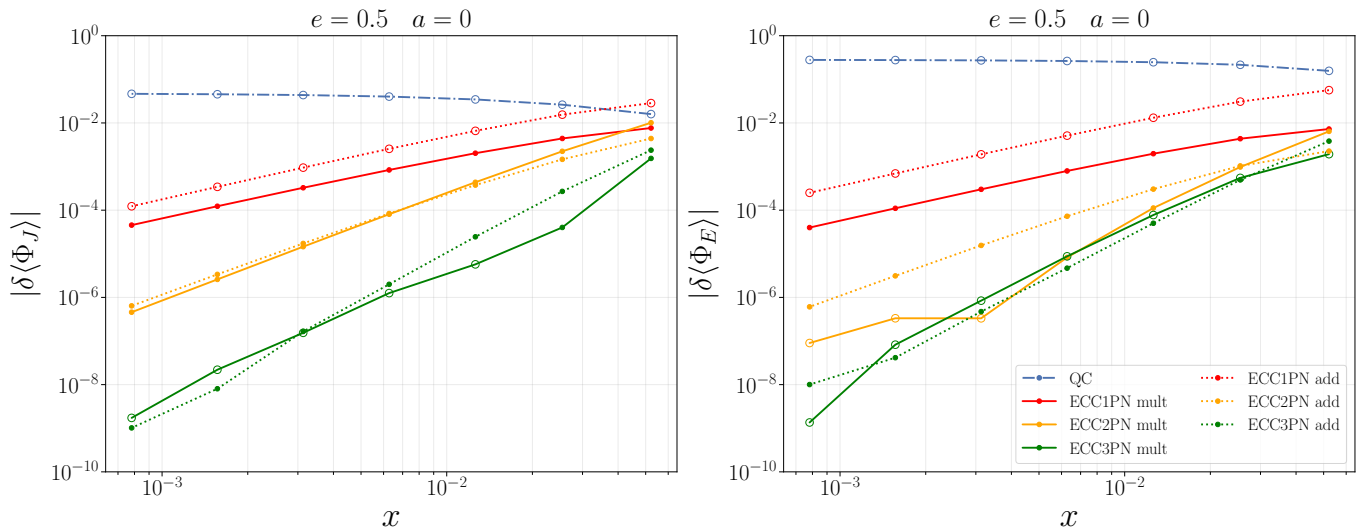
FIG. 2. Absolute value of the fractional differences defined in Eq. (22) of the averaged fluxes computed for orbits in the weak-field regime. The x-axis corresponds to the gauge-invariant variable $x = \langle\dot\varphi\rangle^{2/3}$. The orbits are characterized by the parameters $e = 0.5$, $a = 0$ and $p = \{960, 480, 240, 120, 60, 30, 15\}$. Dotted lines correspond to the additive implementation (add) while solid ones correspond to the multiplicative (mult). Empty circle dots represent negative values of the fractional differences, highlighting zero crossing in the log-log plots.

For the study, we consider the averaged fluxes over one radial period T_r, given by:

$$\langle\Phi_{E,J}\rangle = \frac{1}{T_r}\int_{t_0}^{t_0+T_r} dt\ \Phi_{E,J}\ . \qquad (21)$$

The averaging eliminates the ambiguity due to the Schott terms contribution in the instantaneous-fluxes expressions (20), as the Schott terms appear as total time derivatives.

We consider a set of bound orbits defined by eccentricity $e = 0.5$, spin $a = 0$ and decreasing semilatera recta $p = \{960, 480, 240, 120, 60, 30, 15\}$. This choice allows us to explore the weak-field regime in order to check whether the flux residuals, obtained by subtracting the eccentric corrections (6a) and (6b) from the numerical fluxes, have the expected PN scaling.

In Fig. 2, we show the fractional difference of the averaged numerical fluxes with respect to the averaged analytical fluxes

$$\delta\langle\Phi_{E,J}\rangle = \frac{\langle\Phi_{E,J}^{\text{numerical}}\rangle - \langle\Phi_{E,J}^{\text{analytical}}\rangle}{\langle\Phi_{E,J}^{\text{numerical}}\rangle} \qquad (22)$$

computed on these orbits for different values of the gauge-invariant quantity x defined by

$$x = \langle\dot\varphi\rangle^{2/3}\ . \qquad (23)$$

For the different PN corrections, we follow the same nomenclature used in Fig. 1, and we consider both implementations: solid lines correspond to the multiplicative RR force from Eq. (6a) while dotted lines correspond to the additive RR force from Eq. (6b).

We observe that the eccentric corrections to the RR force provide a consistent improvement over the QC force. For orbits that are in the weakest regimes, $x \approx 8 \times 10^{-4}$, including the ECC3PN corrections improves the agreement with the numerical flux by a factor $\sim 10^8$ over the QC flux. We also find that the curves follow the general expected scaling at low x. The fractional difference between the QC analytical and the Teukolsky flux approaches a constant in the weak field regime, indicating that the QC prescription already needs corrections at the leading "Newtonian" order. The slopes of fractional residuals, after subtracting the ECCnPN corrections in the log-log plot of Fig. 2, are compatible with the expected $x^{-(n+1/2)}$ behavior of a residual that starts at $(n + 1/2)$PN order.

Since for the instantaneous flux comparison in Sec. III A the inclusion of the PN tail corrections did not lead to an unequivocal improvement of the flux, we also considered the effects of omitting the PN tail terms on the orbit-averaged flux. Without providing an explicit plot, we report that the inclusion of these terms is essential in order to recover the expected PN scaling of Fig. 2, corroborating the hypothesis that degradations of higher-order terms in the instantaneous fluxes may come from the Schott terms and disappear when orbit averaging.

When moving into the stronger-field regimes (i.e. for higher values of x), the discrepancy between analytical and numerical averaged fluxes increases, as expected due to the PN nature of the analytical fluxes.

In order to assess the RR force over a wider region of the parameter space, we consider more orbits with different eccentricities spanning the milder and stronger field regimes. Figure 3 shows the fractional differences of
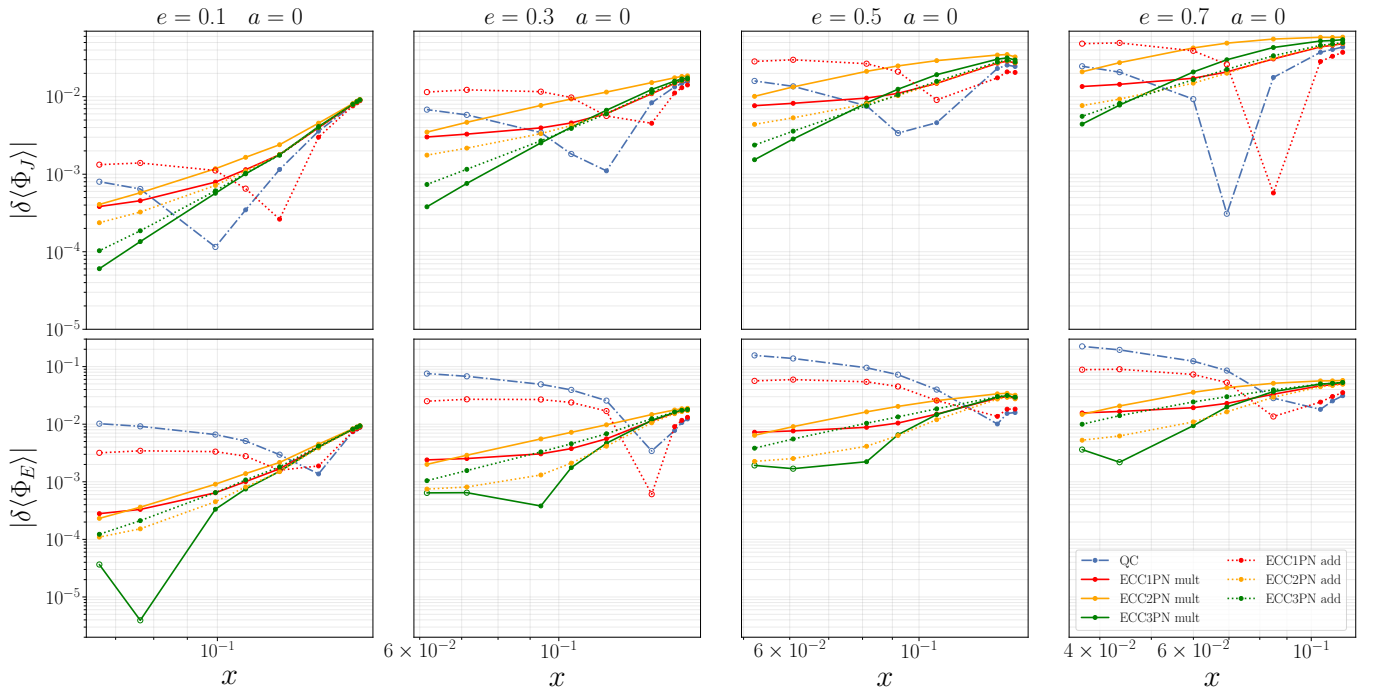
FIG. 3. Absolute value of the fractional differences of the averaged fluxes computed on orbits in mild/strong-field regimes. The orbits with highest x (last points on the right) are characterized by a semilatus rectum $p = p_{\text{LSO}} + 0.025$. The nomenclature is the same as in Fig. 2.

the fluxes evaluated at geodesics with eccentricities $e = \{0.1, 0.3, 0.5, 0.7\}$, spin $a = 0$ and semilatera recta $p = \{p_{\text{LSO}} + 0.025, p_{\text{LSO}} + 0.05, p_{\text{LSO}} + 0.1, 7, 8, 9, 10, 13, 15\}$ [1], where p_{LSO} corresponds to the semilatus rectum of the last stable orbit (LSO) with the corresponding e. For Schwarzschild geodesics this is given by

$$p_{\text{LSO}} = 6 + 2e . \tag{24}$$

The strong-field residuals in Fig. 3 show a much less organized picture than their weak-field counterparts in Fig. 2. There is not always a clear order-by-order improvement from adding higher PN eccentric corrections. This signifies (the start of) the breakdown of the convergence of the PN series in this regime. Notably, the QC and ECC1PN fluxes seemingly outperform the higher-order corrections for larger x. In fact—contrary to naive expectation—the residuals from the QC and ECC1PN fluxes actually decrease, for both the angular-momentum and energy fluxes, up to certain values of x. This behavior is evident starting from values of $x \approx 0.06$ for the orbits with $e = \{0.1, 0.3, 0.5\}$ and of $x \approx 0.04$ for the ones with $e = 0.7$. This decreasing trend is interrupted at larger values of x, where the QC and ECC1PN residuals of the fluxes start to monotonically increase up to the closest

orbits to the LSO with $p = p_{\text{LSO}} + 0.025$. We find that this is connected to a change in sign of the fractional differences between the analytical/numerical fluxes. Since the absolute fractional differences are plotted in Fig. 3, here we represent this change of sign by using different dots: filled dots for positive values of the relative difference (22), empty dots for negative values. This change of sign signifies that in the weak field the average QC fluxes overestimate the average numerical flux, while they underestimate it in the strong field. Consequently, there are some "goldilocks" configurations for which the QC (and ECC1PN) fluxes are "just right", and by coincidence produce the correct flux.

We do not observe a significant difference between the multiplicative and additive implementations in the non-spinning case. However, in Sec. III C we show that this changes when considering spin.

We also find that larger eccentricity values impact the accuracy of the analytical averaged fluxes. More specifically, we observe that for similar values of the x parameter, the relative differences are more prominent for higher eccentricities. This trend is due to the fact that the peri-center of the orbits—where most radiation is generated—is pushed more and more in the strong-field regime, where in turn, the PN expressions are less reliable.

Figure 3 allows us to gauge the overall performance of the flux approximations: in the worst case scenario (i.e. for orbits with $e = 0.7$ and close to the LSO), we observe a difference of $\approx 5\%$, when considering the ECC3PN fluxes.

---

[1] For the orbits with $e = \{0.5, 0.7\}$, we consider the set $p = \{p_{\text{LSO}} + 0.025, p_{\text{LSO}} + 0.05, p_{\text{LSO}} + 0.1, 8, 9, 10, 13, 15\}$, since $p_{\text{LSO}} \geq 7$ for these orbits.
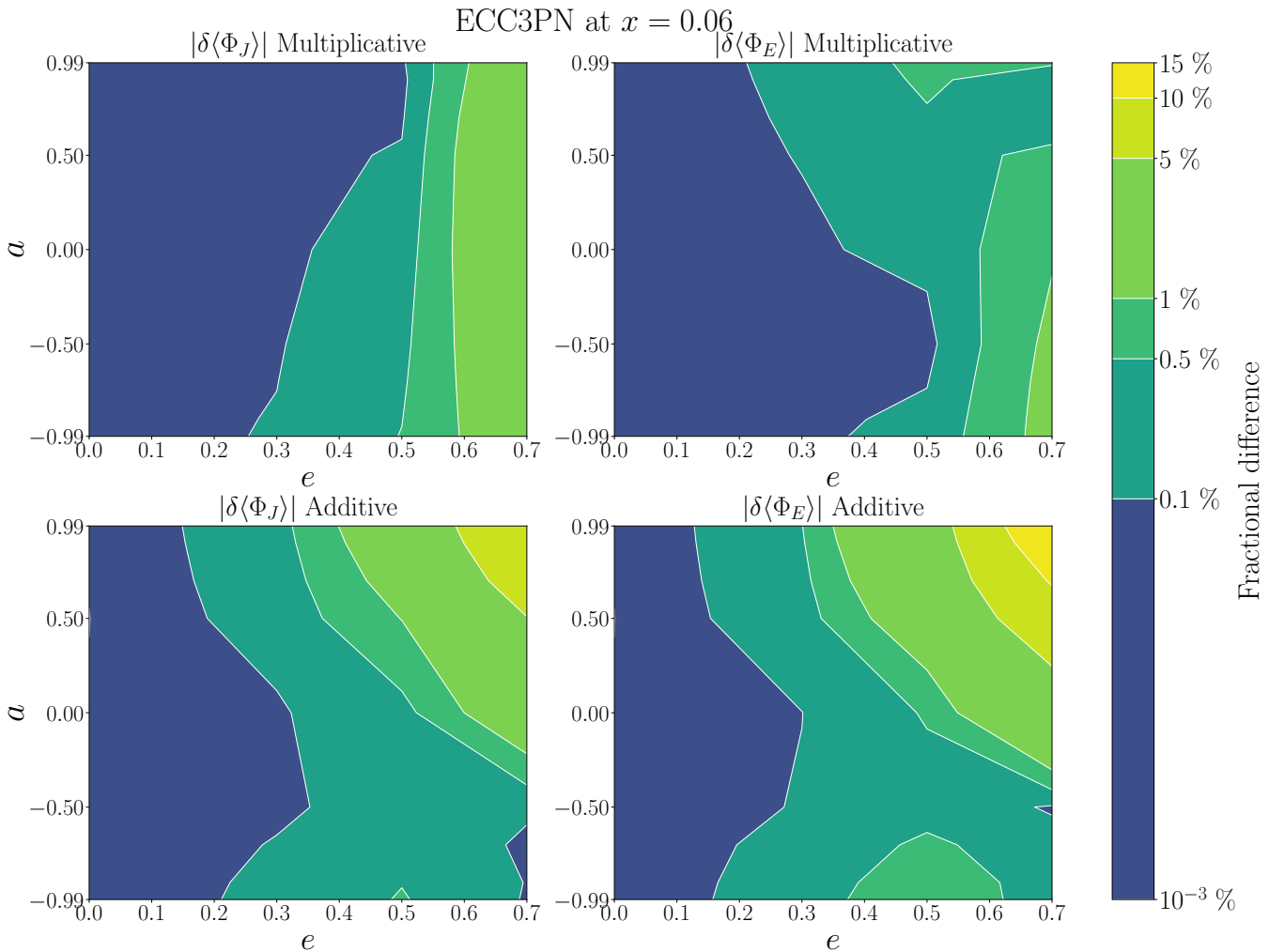
FIG. 4. Contour plots of the absolute value of the fractional differences of the ECC3PN averaged fluxes with respect to the numerical one. They are computed on orbits that span the parameter space (e, a) with fixed value $x = 0.06$. The upper panels show the multiplicative implementation while the lower ones show the additive implementation. The multiplicative implementation shows a worst case scenario of 5% relative difference for higher eccentric spinning prograde orbits.

C. Averaged fluxes: bound orbits in Kerr

So far, we have shown a comparison between analytical and numerical fluxes for eccentric (bound) orbits of a TM moving on geodesics around a Schwarzschild BH. In this section, we provide results that assess the RR force corrections in Eqs. (6) when we allow the central BH to have a spin aligned or antialigned (henceforth, for simplicity aligned) with the orbital angular momentum (i.e., we consider eccentric-equatorial orbits around a Kerr BH).

To test the spinning case, we consider orbits with a fixed value of the x parameter defined in Eq. (23). This choice allows us to identify in a gauge-invariant manner different gravitational-field regimes. The orbits we analyze have eccentricity values $e = \{0.0, 0.1, 0.3, 0.5, 0.7\}$ and spins of the central BH $a = \{-0.99, -0.9, -0.7, -0.5, 0, 0.5, 0.7, 0.9, 0.99\}$.

In Fig. 4, we show contour plots of the fractional difference of the averaged fluxes (21) with respect to the eccentricity and the spin values for orbits with fixed $x = 0.06$. We choose this value for x since it allows computing stable geodesics all over the subset of the parameter space $\{e, a\}$ we want to investigate. We consider the 3PN order in the eccentric sector, ECC3PN, for both implementations (6a) and (6b).

We observe that, regardless of the spin values, for small eccentricities ($e \leq 0.3$), the fractional difference is less than 0.5% for both resummations. When considering higher values of e, the differences increase. This trend corroborates what we mentioned at the end of Sec. III B, notably, for fixed values of x, larger eccentricities degrade the accuracy of the analytical-averaged fluxes, because the pericenter of the orbit is pushed more in the strong-field regime. This degradation increases when considering prograde orbits with high-spin values, for which

the pericenter is even closer to the central BH. For these orbits, we find that the multiplicative implementation provides a mismatch of the fluxes less than 5%, for the considered portion of parameter space. In comparison, the additive implementation provides relative differences that are less than 15%. In particular, we find that for more extreme orbits (i.e., for the ones with high eccentricity and spin), the multiplicative implementation improves over the additive one by a 10% difference.

As a final remark, we mention an overall general improvement of the multiplicative ECC3PN factorization with respect to the additive ECC3PN factorization for regimes with $x \leq 0.06$ over the parameter space (e, a) for both the energy and angular-momentum fluxes. This can be seen in Fig. 7 in Appendix A 4 where we show the behavior of the fluxes at different PN orders, for both factorizations, from weak-field regimes up to strong-field regimes with $x = 0.06$. The considered orbits use the particular configuration of eccentricity and spin of Fig. 4, $e = 0.5$ and prograde spin $a = 0.9$, with semilatera recta $p = \{960, 480, 240, 120, 60, 30, 15\}$. Figure 7 also highlights (as in Fig. 2) the convergence of the different PN truncations of the eccentric fluxes pointing out the correctness of the procedure (and of the expressions) used to derive the EOB eccentric RR force in Eq. (6) in the general spinning scenario. We performed this same test for other eccentricity and spin configurations (e, a) of Fig. 4, finding similar results.

D. Scattering orbits in Schwarzschild

Finally, we push the comparison of the eccentric analytical and numerical fluxes to even higher eccentricities to the $e > 1$ regime (i.e., hyperbolic-scattering orbits). In this section, we restrict our attention to non-spinning Schwarzschild BHs.

We consider hyperbolic orbits with fixed energy $E_0 = 1.005$, and we vary the angular momentum J_0. Figure 5 shows the five different orbits we consider. To produce them, we examine different values of the angular momenta by first computing the critical value J_c through Eq. (6) of Ref. [90]. This critical angular momentum represents the smallest value a TM with fixed energy must have to still scatter back to infinity without plunging into the central BH. For the chosen value of E_0, it is $J_c = 4.0397$. We consider different values for $J_0 = \{J_c + 2, J_c + 0.7, J_c + 0.2, J_c + 0.07, J_c + 0.02\}$, which provide orbits with increasing scattering angle and decreasing pericenter distance. As in the bound case, we compute the analytical and numerical fluxes on these orbits. The numerical fluxes are obtained through the TD Teukolsky code of Refs. [81–83] as mentioned in Sec. II B, while the analytical fluxes are computed similarly to the bound-orbits case (i.e., by evaluating Eqs. (20) on the hyperbolic geodesics). In the following, we consider only the multiplicative implementation (6a), since in Fig. 4 we observe it improves over the additive one.

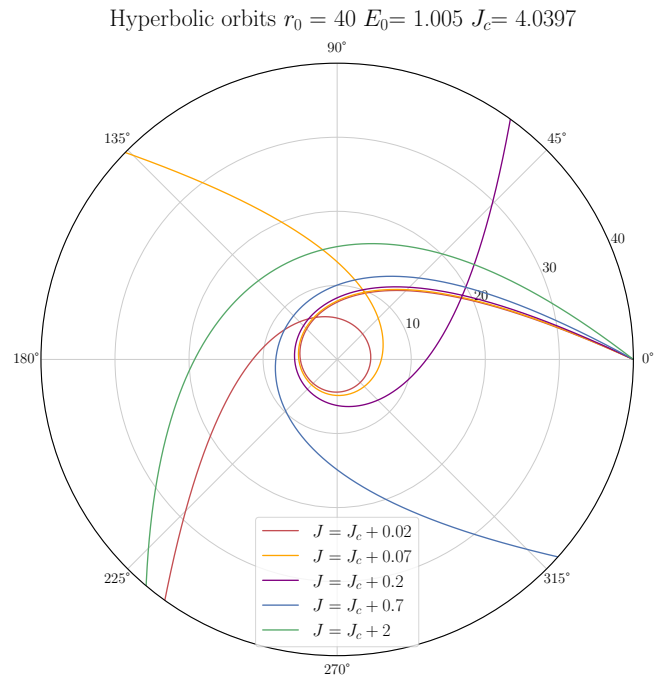Hyperbolic orbits $r_0 = 40$ $E_0 = 1.005$ $J_c = 4.0397$

FIG. 5. The hyperbolic orbits of a TM around a Schwarzschild BH considered in our analysis. They all have energy $E_0 = 1.005$ and critical angular momentum $J_c = 4.0397$. We consider five orbits which have total angular momenta $J_0 = \{J_c + 0.02, J_c + 0.07, J_c + 0.2, J_c + 0.7, J_c + 2\}$.

In Table I, we compare the analytical/numerical total energy and angular momentum emitted by the TM on the examined orbits. These quantities are evaluated by integrating the fluxes on each orbit and truncating at different PN orders. As in the case of the averaged fluxes for bound orbits (see Sec. III B), we also find that the eccentric corrections improve the agreement with the numerical fluxes with respect to the QC case. We observe an improvement of the PN series in the eccentric sector, especially for orbits with smaller J_0. In almost all the examined cases, the 3PN corrections provide the best approximation of the total radiated energy and angular momentum with respect to the numerical flux. However, we find that the fractional differences for the orbits with smaller J_0 ($J_0 = 4.0597$ and $J_0 = 4.1097$) are greater than 10%. This is expected, because these orbits have angular momentum close to the critical one J_c and are characterized by strong-field regimes, where the PN expansions start to breakdown. For the orbits with larger angular momentum, characterized by weaker-field regimes, the residuals are smaller ($\leq 8\%$) but we do not observe a large improvement of the PN series when increasing the order in general. Moreover, for the trajectory with higher angular momentum ($J_0 = 6.0397$), we observe a slight deterioration of the PN series, with the eccentric 1PN corrections providing the best approximation. We believe this is because even in the far weak field these orbits still have high (relativistic) velocities.

TABLE I. Comparison of the analytical/numerical total emitted energy and angular momentum for the different hyperbolic orbits shown in Fig. 5. The analytical fluxes are computed with the multiplicative implementation (6a). For each orbit with energy E_0 and angular momentum J_0, we show the values of the pericenter distance r_p, the numerical total emitted energy E_{Teuk} and angular-momentum J_{Teuk}, and the fractional differences between the analytical emitted energy/angular-momentum, truncated at different PN orders in the eccentric sector, and the total numerical fluxes.

| E_0	J_0	r_p	E_{Teuk}	δE_{QC}	δE_{1PN}	δE_{2PN}	δE_{3PN}	J_{Teuk}	δJ_{QC}	δJ_{1PN}	δJ_{2PN}	δJ_{3PN}
1.005	4.0597	4.39	2.605×10^{-1}	0.3304	0.2095	0.2122	0.1330	2.805	0.2121	0.1948	0.1637	0.0998
1.005	4.1097	4.83	1.450×10^{-1}	0.3316	0.1571	0.1650	0.0964	1.818	0.1701	0.1433	0.1135	0.0593
1.005	4.2397	5.64	6.680×10^{-2}	0.3523	0.1056	0.1204	0.0807	1.062	0.1318	0.0927	0.0711	0.0412
1.005	4.7397	8.14	1.381×10^{-2}	0.4282	0.0473	0.0673	0.0631	3.836×10^{-1}	0.0964	0.0394	0.0357	0.0370
1.005	6.0397	14.67	1.477×10^{-3}	0.5225	0.0065	0.0093	0.0103	9.761×10^{-2}	0.0911	0.0159	0.0224	0.0280
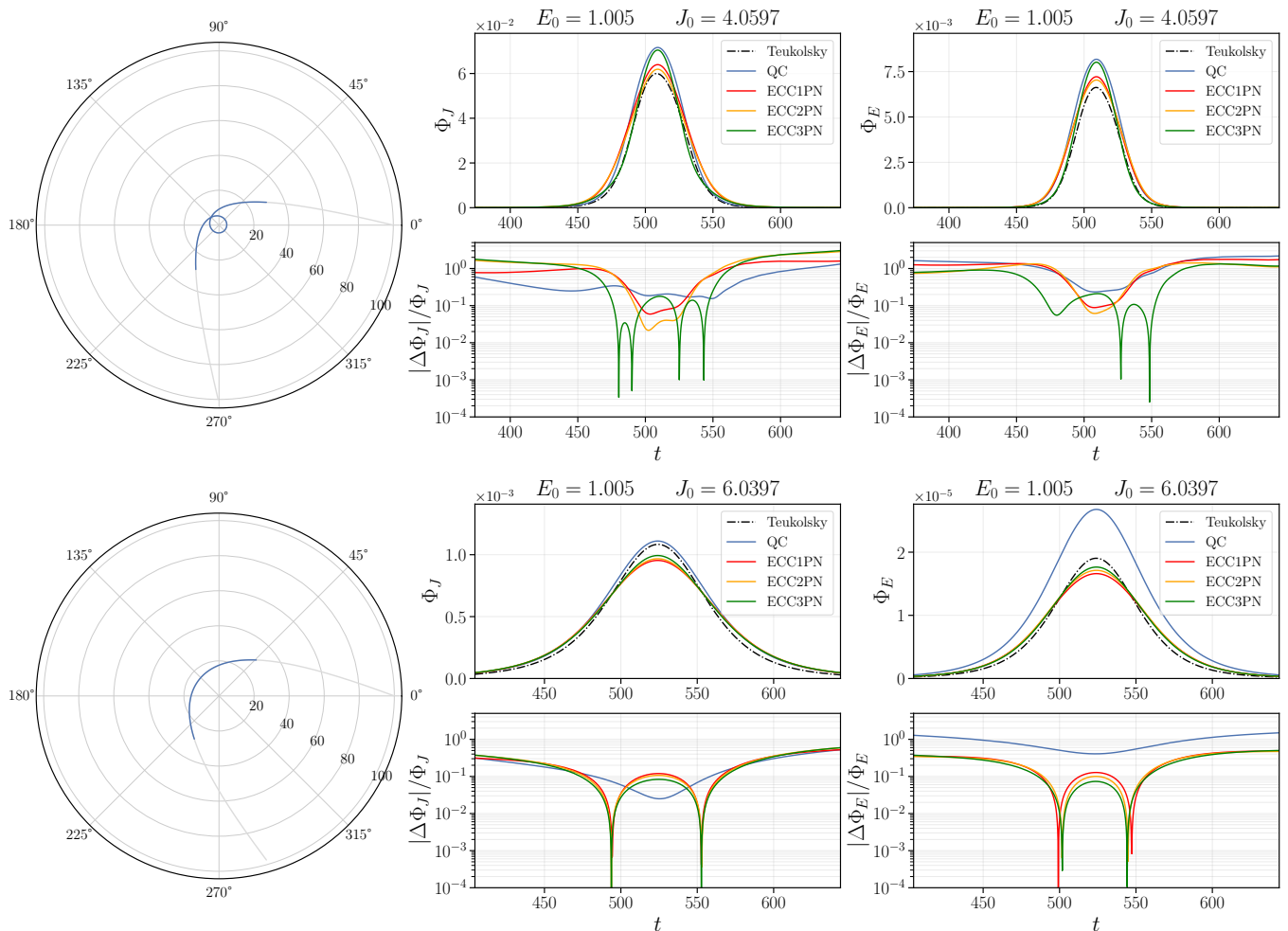
FIG. 6. Instantaneous fluxes for hyperbolic orbits with $E_0 = 1.005$ and $J_0 = \{4.0597, 6.0397\}$. Black curves are the numerical fluxes, blue-dotted ones represent QC fluxes, red curves are the fluxes containing 1PN eccentric corrections while orange and green curves are the eccentric 2PN and 3PN corrected fluxes. The portion of orbit we consider is highlighted in light-blue in the orbit-plot and it is for $r < 30$.

To provide an intuitive picture of this last point we consider again the instantaneous fluxes. Figure 6 shows the time-dependent fluxes for the hyperbolic encounters with the highest ($J_0 = 4.0597$) and smallest ($J_0 = 6.0397$) scattering angle. From the plots, we observe that for the orbit with the highest scattering angle, in the mild/weak-field regime part of the orbits (when $r > 20$), the analytical fluxes differ by $> 80\%$ from the numerical ones. This

is particularly evident for the ECC2PN and ECC3PN fluxes, for which the fractional difference is $> 100\%$. We observe a similar pattern for the orbit with the smallest scattering angle ($J_0 = 6.0397$) (i.e., in the weak-field regime), a large mismatch between the numerical and the analytical curves arises. This large fractional difference we observe for $r > 20$ is caused by the fact that, for hyperbolic orbits, considering the weak-gravitational-field regime does not necessarily correspond to considering small velocities ($v \ll 1$) of the TM. This large-velocity regime deteriorates the convergence of the PN expansion, as shown in the last line of Table I.

IV. CONCLUSIONS

In this work, we tested an EOB eccentric RR force computed with the same procedure as Ref. [60] with a different gauge choice for the leading PN order. The non-spinning 3PN part of this RR force is derived in Ref. [64] while the SO and SS contributions, at 1.5PN and 2PN respectively, are similar to the ones of Ref. [60] but computed taking into account the different gauge choice of the leading order. We considered two possible resummations of this force: a multiplicative (6a) and an additive (6b) one. The assessment of the resummations is performed by considering a TM orbiting the equatorial plane of a Kerr BH. We computed the analytical energy and angular-momentum fluxes, which are linked to the RR force through the balance equations (20), on eccentric geodesics of the Kerr metric, and we compared them with the numerical fluxes computed through the use of a FD [80] and a TD [81–83] Teukolsky codes. We focused our analysis on the orbit-averaged fluxes for bound orbits and on the emitted energy and angular momentum for hyperbolic orbits. This is because when integrating the fluxes over an orbit, we are sure that any degradation coming from the PN-expanded Schott terms is integrated out and we can test the RR force resummations.

When considering bound orbits in the weak-field limit, we recovered the expected scaling of the different PN truncations of the fractional difference of the averaged fluxes, indicating that the procedure used to compute the RR force and its resummed expressions are both correct. We also showed that the eccentric corrections to the RR force are necessary to improve the QC fluxes in this regime. This improvement over the QC fluxes is of the order of 10^8 when considering the ECC3PN fluxes for orbits with $x \approx 10^{-3}$. For non-spinning bound orbits in stronger-field regimes, computed up to the LSO, we found that the fractional differences of the averaged fluxes are $< 5\%$ for eccentricity up to $e = 0.7$. This result holds for both the multiplicative and additive resummations.

For the more general case of bound equatorial geodesics of a Kerr BH, characterized by $x \leq 0.06$, $e = [0, 0.7]$ and $a = [-0.99, 0.99]$, we found that for $e < 0.3$ the fluxes discrepancies are $< 0.5\%$ for both resummations. For larger

eccentricities up to $e = 0.7$, we showed that the multiplicative implementation provides discrepancies with the numerical fluxes that are $< 5\%$, while for the additive implementation, we found larger fractional differences, up to $\approx 15\%$ values. This indicates that, in the considered part of the parameter space, the multiplicative resummation (6a) is a better approximation of the fluxes up to regimes with $x = 0.06$. This is especially true for highly-eccentric ($e = 0.7$) and prograde orbits with large Kerr spin ($a = 0.99$).

Finally, we concluded our analysis by considering geodesic hyperbolic orbits with fixed energy $E = 1.005$ and different angular momenta. We found that the 3PN eccentric corrections of the multiplicative resummation improve the total emitted energy and angular momentum for hyperbolic encounters with angular momenta closer to the critical one. However, for these orbits, the relative differences at 3PN are larger than 8%, due to the strong-field regimes characterizing them. For the unbound orbits in weaker-field regimes, we found smaller values of the fractional differences ($< 7\%$) of the emitted energy and angular momentum. However, we observed a deterioration of the convergence of the PN series, with the 3PN corrections providing higher discrepancies. We pointed out this may be due to the fact that for unbound orbits the weak–gravitational-field regime does not necessarily imply small velocities, impacting the convergence of the eccentric PN orders.

The results we found for the unbound case indicate that the RR force should be further improved for large eccentricities and high velocities. There are possible different strategies to tackle this last point: one possibility is to determine whether different parametrizations improve the results we find. Another strategy could be to perform a further resummation of the eccentric corrections to the RR force $F_{r/\varphi}^{\rm ecc}$ in Eqs. (6). A different approach would be to numerically inform the eccentric corrections by introducing terms that fit the numerical fluxes in the parameter space. We believe all these strategies are promising for improving the EOB eccentric fluxes we studied in this work, and we leave them to future works.

PHY-2307236 and DMS-2309609. Some computations were performed on the UMass-URI UNITY HPC/AI cluster at the Massachusetts Green High-Performance Computing Center (MGHPCC). This work makes use of the Black Hole Perturbation Toolkit [91].

Appendix A: Eccentricity corrections to the RR force

In this Appendix, we summarize the process employed to compute the 3PN eccentric corrections to the QC RR force (7) and the expressions for the Schott energy and angular momentum, in the TM limit. A more detailed procedure and the expressions valid for generic mass ratios will be published in a separate work [64]. However, the main ideas of the calculations are already presented in Refs. [50, 60]. Here, we just outline the basic steps necessary to derive the expressions used in this work.

We start by writing Eqs. (18) and (19) in the form

$$\dot{r}\mathcal{F}_r = -\Phi_E + \dot{\varphi}\Phi_J - \dot{E}_{\text{Schott}} + \dot{\varphi}\dot{J}_{\text{Schott}}, \quad \text{(A1a)}$$

$$\mathcal{F}_\varphi = -\Phi_J - \dot{J}_{\text{Schott}}. \quad \text{(A1b)}$$

Given expressions for the fluxes Φ_E and Φ_J, ansatzes for the Schott terms E_{Schott} and J_{Schott}, and the equations of motion (5), we employ Eqs. (A1) to determine PN expressions for the radial and azimuthal components of the RR force.

More specifically, we employ the complete 3PN expressions of the EOB fluxes presented in Ref. [64]. Then, the free unknown coefficients (gauge constants) appearing in the ansatzes for the Schott terms are determined by imposing the regularity of the radial component of the RR force in the QC limit (this means no $1/p_r$ terms in $\mathcal{F}_r$), and by choosing a specific gauge. Following Refs. [60, 64] we employ a gauge that satisfies

$$\mathcal{F}_\varphi = -\Phi_J + \mathcal{O}(p_r^2), \quad \text{(A2a)}$$

$$\frac{\mathcal{F}_r}{p_r} = \frac{\mathcal{F}_\varphi}{p_\varphi} + \mathcal{O}(p_r^2). \quad \text{(A2b)}$$

With this choice, the QC limit of the resulting RR force

satisfies the gauge used in SEOBNRv5HM, which is given by Eqs. (7).

At leading PN order, the components of the RR force, in a generic gauge, are given by

$$\mathcal{F}_r^{\text{LO}} = \frac{8\nu p_r}{15\,r^3}\left[(-3\alpha + 9\beta + 3)\,p^2 + (9\alpha - 15\beta + 9)\,p_r^2 \right.$$
$$\left. + \frac{9\alpha - 9\beta + 17}{r}\right], \quad \text{(A3a)}$$

$$\mathcal{F}_\varphi^{\text{LO}} = \frac{8\nu p_\varphi}{15\,r^3}\left[9(\alpha+1)\,p_r^2 - 3(2+\alpha)\,p^2 + \frac{3(\alpha-2)}{r}\right], \quad \text{(A3b)}$$

where $p^2 = p_r^2 + p_\varphi^2/r^2$, and $\{\alpha, \beta\}$ are gauge constants, representing the gauge freedom in defining the RR force [92, 93]. In particular, the gauge in Eq. (A2) fixes the value of α to be $-16/3$, but leaves β unspecified. As shown in Ref. [64], β needs to equal $-13/2$ to avoid a 2.5PN modification (relative to the leading order) of the QC orbital phase when transforming between harmonic and EOB coordinates. For the expressions of this work, we use the aforementioned values of α and β, to be consistent with Ref. [64]. As a consequence of this, the expressions used here do not follow the RR gauge employed in Ref. [60].

The next step consists in factorizing the RR force in terms of a QC part and an eccentric correction. In this way, given the PN expressions of $\mathcal{F}_\varphi$ and $\mathcal{F}_r$, and the QC part given by Eqs. (7), we determine the different PN expressions for $\mathcal{F}_\varphi^{\text{ecc}}$ and $\mathcal{F}_r^{\text{ecc}}$ which are specified in Eqs. (6). The results valid for the TM limit are explicitly shown in Sections A 1 and A 2. Additionally, the expressions for the time derivatives of the Schott terms in the TM limit are shown in Sec. A 3.

In the following subsections, we write the expressions in terms of the variables $\{r, p_{r_*}, v_0\}$, where r is the radial separation, p_{r_*} is the radial momentum conjugate to the tortoise coordinate r_*, and v_0 is given by

$$v_0 = \frac{(1 + \dot{p}_{r_*}r^2)^{1/6}}{\sqrt{r}}\,. \quad \text{(A4)}$$

1. Multiplicative corrections

The expressions of the eccentric corrections for the multiplicative implementation (6a) are given by

$$\mathcal{F}_r^{\text{ecc,mult}} = \mathcal{F}_r^{\text{0PN}} + \mathcal{F}_r^{\text{1PN}} + \mathcal{F}_r^{\text{1.5PN,Tail}} + \mathcal{F}_r^{\text{1.5PN,SO}} + \mathcal{F}_r^{\text{2PN}} + \mathcal{F}_r^{\text{2PN,SS}} + \mathcal{F}_r^{\text{2.5PN,Tail}} + \mathcal{F}_r^{\text{3PN}} + \mathcal{F}_r^{\text{3PN,Tail}}, \quad \text{(A5)}$$

where the expressions of the different PN orders are

$$\mathcal{F}_r^{\text{0PN}} = -\frac{19p_{r_*}^2}{12rv_0^4} - \frac{55}{24r^2v_0^4} + \frac{79rv_0^2}{24}, \quad \text{(A6a)}$$

$$\mathcal{F}_r^{\text{1PN}} = -\frac{19p_{r_*}^4}{36r^4v_0^{10}} - \frac{88p_{r_*}^4}{63rv_0^4} - \frac{131p_{r_*}^2}{72r^5v_0^{10}} + \frac{19}{432}p_{r_*}^2 r^3 v_0^6 - \frac{6851p_{r_*}^2}{224r^2v_0^4} - \frac{617p_{r_*}^2 rv_0^2}{1008} - \frac{52459p_{r_*}^2}{12096rv_0^2} - \frac{55}{36r^6v_0^{10}}$$

$$-\frac{79}{864}r^5v_0^{12}+\frac{823r^3v_0^8}{504}-\frac{52897}{2016r^3v_0^4}+\frac{55r^2v_0^6}{864}-\frac{151855}{24192r^2v_0^2}+\frac{218119rv_0^4}{24192}+\frac{47219v_0^2}{2016}\ ,\tag{A6b}$$

$$\mathcal{F}_r^{1.5\mathrm{PN,Tail}}=\pi\left[\frac{5p_{r_*}^4}{576v_0}+\frac{461p_{r_*}^2}{72rv_0}+\frac{79}{6r^2v_0}-\frac{79}{6}rv_0^5\right]\ ,\tag{A6c}$$

$$\mathcal{F}_r^{1.5\mathrm{PN,SO}}=a\left[\frac{19p_{r_*}^2}{18r^4v_0^7}-\frac{19}{144}p_{r_*}^2r^3v_0^7-\frac{29p_{r_*}^2}{9rv_0}+\frac{79}{288}r^5v_0^{13}+\frac{55}{36r^5v_0^7}-\frac{55}{288}r^2v_0^7-\frac{775}{72r^2v_0}+\frac{659}{72}rv_0^5\right]\ ,\tag{A6d}$$

$$\mathcal{F}_r^{2\mathrm{PN}}=-\frac{95p_{r_*}^6}{432r^7v_0^{16}}-\frac{211p_{r_*}^6}{3024r^4v_0^{10}}+\frac{1013p_{r_*}^6}{864rv_0^4}-\frac{115p_{r_*}^4}{96r^8v_0^{16}}-\frac{1055p_{r_*}^4}{96r^5v_0^{10}}-\frac{52459p_{r_*}^4}{72576r^4v_0^8}+\frac{13p_{r_*}^4r^3v_0^6}{6048}+\frac{605p_{r_*}^4}{84r^2v_0^4}+\frac{1129}{672}p_{r_*}^4rv_0^2$$
$$-\frac{1576531p_{r_*}^4}{508032rv_0^2}-\frac{19p_{r_*}^4}{864}-\frac{155p_{r_*}^2}{72r^9v_0^{16}}-\frac{19p_{r_*}^2r^7v_0^{16}}{15552}-\frac{60605p_{r_*}^2}{2016r^6v_0^{10}}+\frac{19}{336}p_{r_*}^2r^5v_0^{12}-\frac{361691p_{r_*}^2}{145152r^5v_0^8}-\frac{86141p_{r_*}^2r^3v_0^8}{217728}$$
$$-\frac{2683325p_{r_*}^2}{12096r^3v_0^4}+\frac{9343p_{r_*}^2r^2v_0^6}{8064}-\frac{58524917p_{r_*}^2}{677376r^2v_0^2}-\frac{311993p_{r_*}^2rv_0^4}{127008}-\frac{11628649p_{r_*}^2}{451584r}+\frac{155599p_{r_*}^2v_0^2}{4032}-\frac{275}{216r^{10}v_0^{16}}$$
$$+\frac{79r^9v_0^{22}}{31104}+\frac{373r^7v_0^{18}}{12096}-\frac{54101}{3024r^7v_0^{10}}-\frac{55r^6v_0^{16}}{31104}-\frac{151855}{72576r^6v_0^8}+\frac{543029r^5v_0^{14}}{435456}-\frac{1163r^4v_0^{12}}{896}+\frac{3017773r^3v_0^{10}}{1016064}$$
$$-\frac{380027}{2268r^4v_0^4}-\frac{158533859}{2032128r^3v_0^2}+\frac{9287503r^2v_0^8}{435456}-\frac{100860815}{2709504r^2}+\frac{148133911rv_0^6}{2709504}+\frac{626551v_0^2}{4032r}+\frac{141658627v_0^4}{2032128}\ ,$$
$$\tag{A6e}$$

$$\mathcal{F}_r^{2\mathrm{PN,SS}}=a^2\left[-\frac{19p_{r_*}^4}{18r^5v_0^{10}}-\frac{55p_{r_*}^2}{36r^6v_0^{10}}+\frac{19}{192}p_{r_*}^2r^3v_0^8+\frac{131p_{r_*}^2}{72r^3v_0^4}+\frac{19p_{r_*}^2}{6r}-\frac{79}{384}r^5v_0^{14}+\frac{145}{96r^4v_0^4}+\frac{55}{384}r^2v_0^8\right.$$
$$\left.+\frac{55}{12r^2}-\frac{79}{12}rv_0^6+\frac{53v_0^2}{96r}\right],\tag{A6f}$$

$$\mathcal{F}_r^{2.5\mathrm{PN,Tail}}=\pi\left[\frac{5p_{r_*}^6}{6912r^3v_0^7}-\frac{413p_{r_*}^6}{34560v_0}-\frac{5p_{r_*}^4r^4v_0^9}{20736}+\frac{1849p_{r_*}^4}{3456r^4v_0^7}-\frac{413p_{r_*}^4r^2v_0^5}{34560}+\frac{1090127p_{r_*}^4}{241920rv_0}+\frac{13805p_{r_*}^4v_0}{580608}+\frac{935p_{r_*}^2}{432r^5v_0^7}\right.$$
$$-\frac{689p_{r_*}^2r^3v_0^9}{2592}+\frac{261253p_{r_*}^2}{2688r^2v_0}+\frac{25385p_{r_*}^2rv_0^5}{6048}+\frac{198055p_{r_*}^2v_0}{9072r}+\frac{79}{36r^6v_0^7}+\frac{79}{144}r^5v_0^{15}-\frac{1633}{504}r^3v_0^{11}$$
$$\left.+\frac{201715}{2016r^3v_0}-\frac{71}{144}r^2v_0^9+\frac{227293v_0}{5376r^2}-\frac{725615rv_0^7}{16128}-\frac{48563v_0^5}{504}\right],\tag{A6g}$$

$$\mathcal{F}_r^{3\mathrm{PN}}=-\frac{79r^{13}v_0^{32}}{1119744}-\frac{971r^{11}v_0^{28}}{326592}+\frac{19p_{r_*}^2r^{11}v_0^{26}}{559872}+\frac{55r^{10}v_0^{26}}{1119744}-\frac{262097r^9v_0^{24}}{10450944}-\frac{3487p_{r_*}^2r^9v_0^{22}}{1306368}+\frac{141187r^8v_0^{22}}{2612736}$$
$$+\frac{2667851r^7v_0^{20}}{12573792}-\frac{278995p_{r_*}^2r^7v_0^{18}}{5225472}+\frac{4362881r^6v_0^{18}}{10450944}+\frac{313p_{r_*}^4r^7v_0^{16}}{326592}-\frac{1315p_{r_*}^2r^6v_0^{16}}{32256}+\frac{8201430199r^5v_0^{16}}{4389396480}$$
$$-\frac{290025695p_{r_*}^2r^5v_0^{14}}{201180672}-\frac{383131475r^4v_0^{14}}{36578304}-\frac{263p_{r_*}^4r^5v_0^{12}}{2304}-\frac{18791p_{r_*}^2r^4v_0^{12}}{20736}-\frac{318507491r^3v_0^{12}}{85349376}+\frac{19p_{r_*}^4r^4v_0^{10}}{11664}$$
$$-\frac{398293579p_{r_*}^2r^3v_0^{10}}{2194698240}+\frac{39377759509r^2v_0^{10}}{877879296}+\frac{63462257p_{r_*}^4r^3v_0^8}{50295168}+\frac{3081350551p_{r_*}^2r^2v_0^8}{134120448}+\frac{343837498725233rv_0^8}{1351934115840}$$
$$-\frac{2033}{70}rv_0^8\ln r-\frac{33812}{315}rv_0^8\ln v_0-\frac{16906\ln 2}{315}rv_0^8-\frac{71p_{r_*}^6r^3v_0^6}{2268}-\frac{47429p_{r_*}^4r^2v_0^6}{48384}-\frac{2094514621p_{r_*}^2rv_0^6}{341397504}$$
$$+\frac{940303127443v_0^6}{2048385024}+\frac{996721p_{r_*}^2v_0^4}{9216}+\frac{24034505p_{r_*}^4rv_0^4}{4064256}+\frac{15293179v_0^4}{31752r}-\frac{68397359p_{r_*}^4v_0^2}{6531840}-\frac{911609p_{r_*}^6rv_0^2}{598752}$$
$$+\frac{1712p_{r_*}^2v_0^2\ln r}{35r}+\frac{2354v_0^2\ln r}{45r^2}+\frac{16264p_{r_*}^2v_0^2\ln v_0}{315r}+\frac{4708v_0^2\ln v_0}{63r^2}-\frac{551068833699073p_{r_*}^2v_0^2}{3379835289600r}$$

$$+ \frac{2181004862746547v_0^2}{6759670579200r^2} + \frac{8132p_{r_*}^2 v_0^2 \ln 2}{315r} + \frac{2354v_0^2 \ln 2}{63r^2} + \frac{373p_{r_*}^6}{24192} - \frac{15435593p_{r_*}^4}{1053696r} - \frac{13372807411p_{r_*}^2}{25288704r^2}$$

$$- \frac{37892126591}{75866112r^3} + \frac{1305953p_{r_*}^6}{381024rv_0^2} + \frac{136832399p_{r_*}^4}{4064256r^2v_0^2} - \frac{1988331389p_{r_*}^2}{3048192r^3v_0^2} - \frac{2744503025}{5225472r^4v_0^2} + \frac{856p_{r_*}^4 \ln r}{35r^3v_0^4}$$

$$- \frac{23861p_{r_*}^2 \ln r}{630r^4v_0^4} - \frac{24931 \ln r}{630r^5v_0^4} - \frac{135077p_{r_*}^8}{149688rv_0^4} + \frac{32911p_{r_*}^6}{18711r^2v_0^4} - \frac{1193113967p_{r_*}^4}{13305600r^3v_0^4} - \frac{19358154601p_{r_*}^2}{29937600r^4v_0^4}$$

$$- \frac{112700503}{316800r^5v_0^4} + \frac{151855p_{r_*}^6}{6096384r^4v_0^8} - \frac{731665p_{r_*}^4}{48384r^5v_0^8} - \frac{173012543p_{r_*}^2}{4064256r^6v_0^8} - \frac{158804437}{6096384r^7v_0^8} + \frac{3721p_{r_*}^8}{9072r^4v_0^{10}} + \frac{264151p_{r_*}^6}{24192r^5v_0^{10}}$$

$$- \frac{868811p_{r_*}^4}{12096r^6v_0^{10}} - \frac{3011119p_{r_*}^2}{13608r^7v_0^{10}} - \frac{804565}{6804r^8v_0^{10}} - \frac{52459p_{r_*}^6}{217728r^7v_0^{14}} - \frac{63503p_{r_*}^4}{48384r^8v_0^{14}} - \frac{85591p_{r_*}^2}{36288r^9v_0^{14}} - \frac{151855}{108864r^{10}v_0^{14}}$$

$$+ \frac{2465p_{r_*}^8}{18144r^7v_0^{16}} - \frac{930955p_{r_*}^6}{217728r^8v_0^{16}} - \frac{1604525p_{r_*}^4}{72576r^9v_0^{16}} - \frac{102055p_{r_*}^2}{3024r^{10}v_0^{16}} - \frac{840635}{54432r^{11}v_0^{16}} - \frac{95p_{r_*}^8}{972r^{10}v_0^{22}} - \frac{1415p_{r_*}^6}{1944r^{11}v_0^{22}}$$

$$- \frac{655p_{r_*}^4}{324r^{12}v_0^{22}} - \frac{1205p_{r_*}^2}{486r^{13}v_0^{22}} - \frac{275}{243r^{14}v_0^{22}} , \tag{A6h}$$

$$\mathcal{F}_r^{\text{3PN,Tail}} = \frac{5593639p_{r_*}^4}{3150r^3v_0^4} - \frac{1044921875p_{r_*}^4 \ln 5}{12096r^3v_0^4} - \frac{1061386821p_{r_*}^4 \ln 3}{11200r^3v_0^4} + \frac{548384416p_{r_*}^4 \ln 2}{1575r^3v_0^4} - \frac{5}{144}\pi^2 p_{r_*}^4 v_0^2$$

$$- \frac{1870681p_{r_*}^4 v_0^2}{4200} + \frac{208984375p_{r_*}^4 v_0^2 \ln 5}{6048} + \frac{34399323}{800}p_{r_*}^4 v_0^2 \ln 3 - \frac{698109088p_{r_*}^4 v_0^2 \ln 2}{4725} + \frac{703\pi^2 p_{r_*}^2}{18r^4v_0^4}$$

$$- \frac{75221\gamma p_{r_*}^2}{630r^4v_0^4} + \frac{100258619p_{r_*}^2}{117600r^4v_0^4} + \frac{75221p_{r_*}^2 \ln r}{420r^4v_0^4} + \frac{1794069p_{r_*}^2 \ln 3}{112r^4v_0^4} - \frac{51789391p_{r_*}^2 \ln 2}{1890r^4v_0^4} - \frac{103\pi^2 p_{r_*}^2 v_0^2}{6r}$$

$$- \frac{8132\gamma p_{r_*}^2 v_0^2}{315r} - \frac{5498951p_{r_*}^2 v_0^2}{11025r} - \frac{8132p_{r_*}^2 v_0^2 \ln v_0}{105r} - \frac{234009p_{r_*}^2 v_0^2 \ln 3}{28r} + \frac{4368596p_{r_*}^2 v_0^2 \ln 2}{315r} + \frac{413\pi^2}{18r^5v_0^4}$$

$$- \frac{6313\gamma}{90r^5v_0^4} - \frac{109379}{50400r^5v_0^4} + \frac{6313 \ln r}{60r^5v_0^4} - \frac{234009 \ln 3}{560r^5v_0^4} + \frac{176657 \ln 2}{630r^5v_0^4} - \frac{1045\pi^2 v_0^2}{18r^2} + \frac{10379\gamma v_0^2}{630r^2}$$

$$- \frac{9846541v_0^2}{117600r^2} - \frac{33919v_0^2 \ln r}{420r^2} - \frac{2354v_0^2 \ln v_0}{21r^2} + \frac{234009v_0^2 \ln 3}{560r^2} - \frac{267821v_0^2 \ln 2}{630r^2} + \frac{316}{9}\pi^2 rv_0^8$$

$$+ \frac{16906}{315}\gamma rv_0^8 + \frac{6857279rv_0^8}{88200} + \frac{16906}{105}rv_0^8 \ln v_0 + \frac{16906 \ln 2}{105}rv_0^8 , \tag{A6i}$$

where $\gamma \approx 0.577$ is the Euler-gamma constant.

While for the azimuthal component of the RR force we have

$$\mathcal{F}_\varphi^{\text{ecc,mult}} = \mathcal{F}_\varphi^{\text{0PN}} + \mathcal{F}_\varphi^{\text{1PN}} + \mathcal{F}_\varphi^{\text{1.5PN,Tail}} + \mathcal{F}_\varphi^{\text{1.5PN,SO}} + \mathcal{F}_\varphi^{\text{2PN}} + \mathcal{F}_\varphi^{\text{2PN,SS}} + \mathcal{F}_\varphi^{\text{2.5PN,Tail}} + \mathcal{F}_\varphi^{\text{3PN}} + \mathcal{F}_\varphi^{\text{3PN,Tail}} , \tag{A7}$$

with

$$\mathcal{F}_\varphi^{\text{0PN}} = \frac{29p_{r_*}^2}{12rv_0^4} + \frac{11}{6r^2v_0^4} - \frac{5rv_0^2}{6} , \tag{A8a}$$

$$\mathcal{F}_\varphi^{\text{1PN}} = \frac{29p_{r_*}^4}{36r^4v_0^{10}} - \frac{58p_{r_*}^4}{63rv_0^4} + \frac{20p_{r_*}^2}{9r^5v_0^{10}} - \frac{29}{432}p_{r_*}^2 r^3 v_0^6 - \frac{1977p_{r_*}^2}{224r^2v_0^4} - \frac{613}{504}p_{r_*}^2 rv_0^2 + \frac{80069p_{r_*}^2}{12096rv_0^2} + \frac{11}{9r^6v_0^{10}} + \frac{5r^5v_0^{12}}{216}$$

$$+ \frac{557r^3v_0^8}{1008} - \frac{10687}{2016r^3v_0^4} - \frac{11r^2v_0^6}{216} + \frac{30371}{6048r^2v_0^2} - \frac{13805rv_0^4}{6048} + \frac{1643v_0^2}{2016} , \tag{A8b}$$

$$\mathcal{F}_\varphi^{\text{1.5PN,Tail}} = \pi \left[-\frac{49p_{r_*}^6}{1440r^2v_0^7} + \frac{171p_{r_*}^2}{16r^4v_0^7} - \frac{29p_{r_*}^2}{3rv_0} + \frac{167}{48r^5v_0^7} - \frac{109}{16r^2v_0} + \frac{10}{3}rv_0^5 \right] , \tag{A8c}$$

$$\mathcal{F}_\varphi^{\text{1.5PN,SO}} = a \left[\frac{29}{144}p_{r_*}^2 r^3 v_0^7 - \frac{5p_{r_*}^4}{2r^3v_0^7} - \frac{73p_{r_*}^2}{9r^4v_0^7} + \frac{89p_{r_*}^2}{18rv_0} - \frac{5}{72}r^5v_0^{13} - \frac{11}{9r^5v_0^7} + \frac{11}{72}r^2v_0^7 + \frac{215}{72r^2v_0} - \frac{133}{72}rv_0^5 \right] , \tag{A8d}$$

$$\mathcal{F}_\varphi^{\text{2PN}} = \frac{145 p_{r_*}^6}{432 r^7 v_0^{16}} - \frac{2755 p_{r_*}^6}{3024 r^4 v_0^{10}} + \frac{37 p_{r_*}^6}{108 r v_0^4} + \frac{115 p_{r_*}^4}{72 r^8 v_0^{16}} - \frac{6515 p_{r_*}^4}{2016 r^5 v_0^{10}} + \frac{80069 p_{r_*}^4}{72576 r^4 v_0^8} + \frac{493 p_{r_*}^4 r^3 v_0^6}{6048} + \frac{101 p_{r_*}^4}{504 r^2 v_0^4}$$
$$+ \frac{505}{252} p_{r_*}^4 r v_0^2 - \frac{1841587 p_{r_*}^4}{508032 r v_0^2} + \frac{29 p_{r_*}^4}{864} + \frac{85 p_{r_*}^2}{36 r^9 v_0^{16}} + \frac{29 p_{r_*}^2 r^7 v_0^{16}}{15552} - \frac{12755 p_{r_*}^2}{2016 r^6 v_0^{10}} + \frac{71 p_{r_*}^2 r^5 v_0^{12}}{1008} + \frac{13805 p_{r_*}^2}{4536 r^5 v_0^8}$$
$$- \frac{261869 p_{r_*}^2 r^3 v_0^8}{217728} - \frac{797813 p_{r_*}^2}{12096 r^3 v_0^4} - \frac{1355 p_{r_*}^2 r^2 v_0^6}{8064} - \frac{14442791 p_{r_*}^2}{677376 r^2 v_0^2} - \frac{1029853 p_{r_*}^2 r v_0^4}{254016} + \frac{17738551 p_{r_*}^2}{451584 r}$$
$$+ \frac{5311 p_{r_*}^2 v_0^2}{576} + \frac{55}{54 r^{10} v_0^{16}} - \frac{5 r^9 v_0^{22}}{7776} - \frac{419 r^7 v_0^{18}}{12096} - \frac{9119}{3024 r^7 v_0^{10}} + \frac{11 r^6 v_0^{16}}{7776} + \frac{30371}{18144 r^6 v_0^8} + \frac{23543 r^5 v_0^{14}}{108864}$$
$$+ \frac{1373 r^4 v_0^{12}}{8064} - \frac{235303}{18144 r^4 v_0^4} + \frac{1924417 r^3 v_0^{10}}{1016064} - \frac{22858319}{2032128 r^3 v_0^2} - \frac{13733 r^2 v_0^8}{27216} + \frac{20172163}{677376 r^2} - \frac{9304097 r v_0^6}{677376}$$
$$+ \frac{26207 v_0^2}{4032 r} + \frac{516307 v_0^4}{2032128} \,, \tag{A8e}$$

$$\mathcal{F}_\varphi^{\text{2PN,SS}} = a^2 \Bigg[\frac{29 p_{r_*}^4}{18 r^5 v_0^{10}} + \frac{11 p_{r_*}^2}{9 r^6 v_0^{10}} - \frac{29}{192} p_{r_*}^2 r^3 v_0^8 + \frac{755 p_{r_*}^2}{72 r^3 v_0^4} - \frac{29 p_{r_*}^2}{6 r} + \frac{5}{96} r^5 v_0^{14} + \frac{409}{96 r^4 v_0^4} - \frac{11}{96} r^2 v_0^8 \tag{A8f}$$
$$- \frac{11}{3 r^2} + \frac{5}{3} r v_0^6 - \frac{211 v_0^2}{96 r} \Bigg], \tag{A8g}$$

$$\mathcal{F}_\varphi^{\text{2.5PN,Tail}} = \pi \Bigg[\frac{49 p_{r_*}^8}{3456 r^2 v_0^7} - \frac{343 p_{r_*}^8}{17280 r^5 v_0^{13}} - \frac{343 p_{r_*}^6}{8640 r^6 v_0^{13}} - \frac{15361 p_{r_*}^6}{30240 r^3 v_0^7} - \frac{19327 p_{r_*}^6}{207360 r^2 v_0^5} + \frac{49 p_{r_*}^6 r^2 v_0^3}{51840} + \frac{49 p_{r_*}^6}{3456 v_0}$$
$$+ \frac{399 p_{r_*}^4}{64 r^7 v_0^{13}} + \frac{60827 p_{r_*}^4}{5376 r^4 v_0^7} + \frac{1537 p_{r_*}^4}{252 r v_0} + \frac{8351 p_{r_*}^2}{576 r^8 v_0^{13}} + \frac{184447 p_{r_*}^2}{4032 r^5 v_0^7} + \frac{52459 p_{r_*}^2}{1792 r^4 v_0^5} + \frac{29}{72} p_{r_*}^2 r^3 v_0^9 - \frac{19}{64} p_{r_*}^2 v_0^3$$
$$+ \frac{12683 p_{r_*}^2}{504 r^2 v_0} + \frac{1625}{252} p_{r_*}^2 r v_0^5 - \frac{266365 p_{r_*}^2 v_0}{8064 r} + \frac{1169}{288 r^9 v_0^{13}} + \frac{1615}{336 r^6 v_0^7} - \frac{5}{36} \pi r^5 v_0^{15} + \frac{461087}{48384 r^5 v_0^5}$$
$$- \frac{767}{252} r^3 v_0^{11} - \frac{16217}{4032 r^3 v_0} + \frac{503 r^2 v_0^9}{1728} - \frac{1143395 v_0}{48384 r^2} + \frac{45925 r v_0^7}{4032} - \frac{167 v_0^3}{1728 r} + \frac{1151 v_0^5}{1344} \Bigg], \tag{A8h}$$

$$\mathcal{F}_\varphi^{\text{3PN}} = \frac{5 r^{13} v_0^{32}}{279936} + \frac{1957 r^{11} v_0^{28}}{1306368} - \frac{29 p_{r_*}^2 r^{11} v_0^{26}}{559872} - \frac{11 r^{10} v_0^{26}}{279936} + \frac{36403 r^9 v_0^{24}}{2612736} - \frac{1943 p_{r_*}^2 r^9 v_0^{22}}{653184} - \frac{26357 r^8 v_0^{22}}{2612736}$$
$$- \frac{45275695 r^7 v_0^{20}}{201180672} + \frac{17195 p_{r_*}^2 r^7 v_0^{18}}{746496} - \frac{707257 r^6 v_0^{18}}{2612736} - \frac{1247 p_{r_*}^4 r^7 v_0^{16}}{326592} + \frac{4687 p_{r_*}^2 r^6 v_0^{16}}{290304} + \frac{17132501 r^5 v_0^{16}}{31352832}$$
$$+ \frac{74723225 p_{r_*}^2 r^5 v_0^{14}}{100590336} + \frac{915435407 r^4 v_0^{14}}{402361344} - \frac{35}{216} p_{r_*}^4 r^5 v_0^{12} + \frac{23329 p_{r_*}^2 r^4 v_0^{12}}{145152} + \frac{4837213015 r^3 v_0^{12}}{341397504} - \frac{29 p_{r_*}^4 r^4 v_0^{10}}{11664}$$
$$- \frac{8345573611 p_{r_*}^2 r^3 v_0^{10}}{2194698240} + \frac{171479 r^2 v_0^{10}}{22394880} + \frac{86644739 p_{r_*}^4 r^3 v_0^8}{50295168} - \frac{1129077875 p_{r_*}^2 r^2 v_0^8}{134120448} + \frac{118884442364929 r v_0^8}{1689917644800}$$
$$- \frac{214}{35} r v_0^8 \ln r + \frac{1712}{63} r v_0^8 \ln v_0 + \frac{856 \ln 2}{63} r v_0^8 - \frac{5959 p_{r_*}^6 r^3 v_0^6}{72576} + \frac{13715 p_{r_*}^4 r^2 v_0^6}{48384} - \frac{4589832917 p_{r_*}^2 r v_0^6}{170698752}$$
$$- \frac{21850038725 v_0^6}{2048385024} + \frac{32151845 p_{r_*}^2 v_0^4}{1354752} + \frac{295427 p_{r_*}^4 r v_0^4}{42336} + \frac{20710261 v_0^4}{1354752 r} - \frac{193847585 p_{r_*}^4 v_0^2}{14370048} - \frac{3322987 p_{r_*}^6 r v_0^2}{1197504}$$
$$+ \frac{2889 p_{r_*}^2 v_0^2 \ln r}{70 r} - \frac{535 v_0^2 \ln r}{126 r^2} - \frac{24824 p_{r_*}^2 v_0^2 \ln v_0}{315 r} - \frac{18832 v_0^2 \ln v_0}{315 r^2} - \frac{252830224115069 p_{r_*}^2 v_0^2}{675967057920 r} - \frac{9416 v_0^2 \ln 2}{315 r^2}$$
$$+ \frac{41138929379561 v_0^2}{1689917644800 r^2} - \frac{12412 p_{r_*}^2 v_0^2 \ln 2}{315 r} - \frac{1595 p_{r_*}^6}{24192} - \frac{29482781 p_{r_*}^4}{1053696 r} - \frac{2756994649 p_{r_*}^2}{25288704 r^2} - \frac{3565629869}{75866112 r^3}$$
$$+ \frac{12206381 p_{r_*}^6}{6096384 r v_0^2} + \frac{527351 p_{r_*}^4}{193536 r^2 v_0^2} - \frac{560474717 p_{r_*}^2}{3048192 r^3 v_0^2} - \frac{1390812335}{36578304 r^4 v_0^2} - \frac{214 p_{r_*}^4 \ln r}{35 r^3 v_0^4} - \frac{7276 p_{r_*}^2 \ln r}{315 r^4 v_0^4} - \frac{107 \ln r}{18 r^5 v_0^4}$$
$$+ \frac{223 p_{r_*}^8}{37422 r v_0^4} + \frac{23518547 p_{r_*}^6}{5987520 r^2 v_0^4} + \frac{471959591 p_{r_*}^4}{4435200 r^3 v_0^4} - \frac{92174527 p_{r_*}^2}{1871100 r^4 v_0^4} - \frac{1837807}{190080 r^5 v_0^4} - \frac{8727521 p_{r_*}^6}{6096384 r^4 v_0^8} - \frac{17678683 p_{r_*}^4}{4064256 r^5 v_0^8}$$
$$- \frac{29650379 p_{r_*}^2}{4064256 r^6 v_0^8} - \frac{19302151}{6096384 r^7 v_0^8} + \frac{15383 p_{r_*}^8}{18144 r^4 v_0^{10}} + \frac{18511 p_{r_*}^6}{24192 r^5 v_0^{10}} - \frac{145343 p_{r_*}^4}{6048 r^6 v_0^{10}} - \frac{2801305 p_{r_*}^2}{54432 r^7 v_0^{10}} - \frac{133409}{13608 r^8 v_0^{10}}$$

$$+ \frac{80069 p_{r_*}^6}{217728 r^7 v_0^{14}} + \frac{63503 p_{r_*}^4}{36288 r^8 v_0^{14}} + \frac{46937 p_{r_*}^2}{18144 r^9 v_0^{14}} + \frac{30371}{27216 r^{10} v_0^{14}} - \frac{11455 p_{r_*}^8}{18144 r^7 v_0^{16}} - \frac{537295 p_{r_*}^6}{217728 r^8 v_0^{16}} - \frac{324335 p_{r_*}^4}{72576 r^9 v_0^{16}}$$

$$- \frac{970 p_{r_*}^2}{189 r^{10} v_0^{16}} - \frac{110465}{54432 r^{11} v_0^{16}} + \frac{145 p_{r_*}^8}{972 r^{10} v_0^{22}} + \frac{245 p_{r_*}^6}{243 r^{11} v_0^{22}} + \frac{200 p_{r_*}^4}{81 r^{12} v_0^{22}} + \frac{620 p_{r_*}^2}{243 r^{13} v_0^{22}} + \frac{220}{243 r^{14} v_0^{22}} \,, \tag{A8i}$$

$$\begin{aligned}
\mathcal{F}_\varphi^{\text{3PN, Tail}} = & \frac{49 \pi^2 p_{r_*}^6}{360 r^2 v_0^4} + \frac{1870681 p_{r_*}^6}{4200 r^2 v_0^4} - \frac{208984375 p_{r_*}^6 \ln 5}{6048 r^2 v_0^4} - \frac{34399323 p_{r_*}^6 \ln 3}{800 r^2 v_0^4} + \frac{698109088 p_{r_*}^6 \ln 2}{4725 r^2 v_0^4} + \frac{193777 p_{r_*}^4}{420 r^3 v_0^4} \\
& + \frac{234009 p_{r_*}^4 \ln 3}{28 r^3 v_0^4} - \frac{4392992 p_{r_*}^4 \ln 2}{315 r^3 v_0^4} - \frac{1681 \pi^2 p_{r_*}^2}{36 r^4 v_0^4} + \frac{7597 \gamma p_{r_*}^2}{630 r^4 v_0^4} + \frac{29951111 p_{r_*}^2}{352800 r^4 v_0^4} - \frac{7597 p_{r_*}^2 \ln r}{420 r^4 v_0^4} \\
& + \frac{78003 p_{r_*}^2 \ln 3}{560 r^4 v_0^4} - \frac{69443 p_{r_*}^2 \ln 2}{630 r^4 v_0^4} + \frac{232 \pi^2 p_{r_*}^2 v_0^2}{9 r} + \frac{12412 \gamma p_{r_*}^2 v_0^2}{315 r} + \frac{2517229 p_{r_*}^2 v_0^2}{44100 r} + \frac{12412 p_{r_*}^2 v_0^2 \ln v_0}{105 r} \\
& + \frac{12412 p_{r_*}^2 v_0^2 \ln 2}{105 r} - \frac{503 \pi^2}{36 r^5 v_0^4} + \frac{107 \gamma}{630 r^5 v_0^4} - \frac{8511719}{352800 r^5 v_0^4} - \frac{107 \ln r}{420 r^5 v_0^4} + \frac{78003 \ln 3}{560 r^5 v_0^4} - \frac{17441 \ln 2}{126 r^5 v_0^4} + \frac{823 \pi^2 v_0^2}{36 r^2} \\
& + \frac{8453 \gamma v_0^2}{630 r^2} + \frac{4193213 v_0^2}{117600 r^2} + \frac{10379 v_0^2 \ln r}{420 r^2} + \frac{9416 v_0^2 \ln v_0}{105 r^2} - \frac{78003 v_0^2 \ln 3}{560 r^2} + \frac{123157 v_0^2 \ln 2}{630 r^2} - \frac{80}{9} \pi^2 r v_0^8 \\
& - \frac{856}{63} \gamma r v_0^8 - \frac{86801 r v_0^8}{4410} - \frac{856}{21} r v_0^8 \ln v_0 - \frac{856 \ln 2}{21} r v_0^8 \,. \tag{A8j}
\end{aligned}$$

2. Additive RR force eccentric corrections

Here we provide the additive implementation (6b) expressions. For the radial component we have

$$\mathcal{F}_r^{\text{ecc,add}} = \mathcal{F}_r^{\text{0PN}} + \mathcal{F}_r^{\text{1PN}} + \mathcal{F}_r^{\text{1.5PN,Tail}} + \mathcal{F}_r^{\text{1.5PN,SO}} + \mathcal{F}_r^{\text{2PN}} + \mathcal{F}_r^{\text{2PN,SS}} + \mathcal{F}_r^{\text{2.5PN,Tail}} + \mathcal{F}_r^{\text{3PN}} + \mathcal{F}_r^{\text{3PN,Tail}} \,, \tag{A9}$$

where the different terms are

$$\mathcal{F}_r^{\text{0PN}} = \frac{152 p_{r_*}^3}{15 r^3} + \frac{44 p_{r_*}}{3 r^4} + \frac{32 p_{r_*} v_0^4}{5 r^2} - \frac{316 p_{r_*} v_0^6}{15 r} \,, \tag{A10a}$$

$$\begin{aligned}
\mathcal{F}_r^{\text{1PN}} = & \frac{372 p_{r_*}^5}{35 r^3} - \frac{32 p_{r_*}^3}{15 r^5 v_0^2} + \frac{21547 p_{r_*}^3}{105 r^4} + \frac{16 p_{r_*}^3 v_0^4}{15 r^2} + \frac{44 p_{r_*}^3 v_0^6}{21 r} - \frac{64 p_{r_*}}{15 r^6 v_0^2} + \frac{6369 p_{r_*}}{35 r^5} + \frac{8}{45} p_{r_*} r^2 v_0^{14} \\
& - \frac{51971 p_{r_*} v_0^6}{315 r^2} - \frac{1466}{105} p_{r_*} r v_0^{12} + \frac{16 p_{r_*} v_0^{10}}{15} \,, \tag{A10b}
\end{aligned}$$

$$\mathcal{F}_r^{\text{1.5PN,Tail}} = \pi \left[-\frac{p_{r_*}^5 v_0^3}{18 r^2} - \frac{4 p_{r_*}^3 v_0^3}{9 r^3} - \frac{128 p_{r_*} v_0^3}{5 r^4} + \frac{128 p_{r_*} v_0^7}{5 r^2} \right] \,, \tag{A10c}$$

$$\mathcal{F}_r^{\text{1.5PN,SO}} = a \left[-\frac{32 p_{r_*}^3 v_0^3}{5 r^3} + \frac{64 p_{r_*} v_0}{15 r^5} + \frac{236 p_{r_*} v_0^3}{15 r^4} - \frac{8}{15} p_{r_*} r^2 v_0^{15} - \frac{256 p_{r_*} v_0^7}{15 r^2} - \frac{12 p_{r_*} v_0^9}{5 r} \right] \,, \tag{A10d}$$

$$\begin{aligned}
\mathcal{F}_r^{\text{2PN}} = & -\frac{2116 p_{r_*}^7}{315 r^3} - \frac{8 p_{r_*}^5}{45 r^8 v_0^8} + \frac{56 p_{r_*}^5}{45 r^5 v_0^2} - \frac{1468 p_{r_*}^5}{105 r^4} - \frac{4 p_{r_*}^5 v_0^4}{9 r^2} - \frac{1619 p_{r_*}^5 v_0^6}{210 r} - \frac{32 p_{r_*}^3}{45 r^9 v_0^8} - \frac{128 p_{r_*}^3}{45 r^6 v_0^2} + \frac{1440472 p_{r_*}^3}{945 r^5} \\
& + \frac{152 p_{r_*}^3 v_0^4}{45 r^3} - \frac{16}{135} p_{r_*}^3 r^2 v_0^{14} - \frac{151853 p_{r_*}^3 v_0^6}{630 r^2} + \frac{137}{35} p_{r_*}^3 r v_0^{12} - \frac{28 p_{r_*}^3 v_0^8}{135 r} - \frac{16 p_{r_*}^3 v_0^{10}}{45} - \frac{32 p_{r_*}}{45 r^{10} v_0^8} - \frac{32 p_{r_*}}{15 r^7 v_0^2} \\
& + \frac{3403531 p_{r_*}}{2835 r^6} - \frac{16}{135} p_{r_*} r^4 v_0^{20} + \frac{8 p_{r_*} v_0^4}{9 r^4} - \frac{7829}{630} p_{r_*} r^3 v_0^{18} - \frac{908602 p_{r_*} v_0^6}{945 r^3} - \frac{16}{105} p_{r_*} r^2 v_0^{16} - \frac{159268 p_{r_*} v_0^8}{2835 r^2} \\
& + \frac{52}{45} p_{r_*} r v_0^{14} + \frac{64 p_{r_*} v_0^{10}}{15 r} - \frac{109397 p_{r_*} v_0^{12}}{630} \,, \tag{A10e}
\end{aligned}$$

$$\mathcal{F}_r^{\text{2PN,SS}} = a^2 \left[-\frac{64 p_{r_*}^3}{15 r^6 v_0^2} - \frac{116 p_{r_*}^3}{15 r^5} - \frac{73 p_{r_*}}{3 r^6} - \frac{32 p_{r_*} v_0^4}{5 r^4} + \frac{263 p_{r_*} v_0^6}{15 r^3} + \frac{2}{5} p_{r_*} r^2 v_0^{16} + \frac{64 p_{r_*} v_0^8}{5 r^2} \right], \tag{A10f}$$

$$\mathcal{F}_r^{\text{2.5PN,Tail}} = \pi \left[\frac{p_{r_*}^7}{72 r^5 v_0^3} + \frac{121 p_{r_*}^7 v_0^3}{1800 r^2} + \frac{5 p_{r_*}^5}{36 r^6 v_0^3} - \frac{41429 p_{r_*}^5 v_0^3}{12600 r^3} + \frac{121 p_{r_*}^5 v_0^9}{1800} + \frac{298 p_{r_*}^3}{45 r^7 v_0^3} - \frac{224 p_{r_*}^3 v_0}{15 r^5} + \frac{81259 p_{r_*}^3 v_0^3}{420 r^4} - \frac{p_{r_*}^3 v_0^9}{3 r} \right.$$
$$\left. - \frac{32 p_{r_*}^3 v_0^7}{15 r^2} + \frac{64 p_{r_*}}{5 r^8 v_0^3} - \frac{448 p_{r_*} v_0}{15 r^6} + \frac{2467 p_{r_*} v_0^3}{21 r^5} + \frac{96 p_{r_*} v_0^7}{5 r^3} + \frac{16}{45} p_{r_*} r^2 v_0^{17} - \frac{37117 p_{r_*} v_0^9}{315 r^2} - \frac{32}{15} p_{r_*} v_0^{13} \right], \tag{A10g}$$

$$\mathcal{F}_r^{\text{3PN}} = \frac{15017 p_{r_*}^9}{3465 r^3} - \frac{16 p_{r_*}^7}{405 r^{11} v_0^{14}} + \frac{32 p_{r_*}^7}{135 r^8 v_0^8} - \frac{124 p_{r_*}^7}{135 r^5 v_0^2} - \frac{666419 p_{r_*}^7}{27720 r^4} + \frac{22 p_{r_*}^7 v_0^4}{81 r^2} + \frac{37519 p_{r_*}^7 v_0^6}{6930 r} - \frac{32 p_{r_*}^5}{135 r^{12} v_0^{14}} + \frac{8 p_{r_*}^5}{135 r^9 v_0^8}$$
$$+ \frac{52 p_{r_*}^5}{15 r^6 v_0^2} + \frac{503253523 p_{r_*}^5}{519750 r^5} - \frac{27392 p_{r_*}^5 \ln r}{175 r^5} + \frac{28 p_{r_*}^5 v_0^2}{405 r^4} - \frac{70 p_{r_*}^5 v_0^4}{27 r^3} + \frac{8}{81} p_{r_*}^5 r^2 v_0^{14} + \frac{19473 p_{r_*}^5 v_0^6}{700 r^2} - \frac{22301 p_{r_*}^5 r v_0^{12}}{2310}$$
$$+ \frac{119 p_{r_*}^5 v_0^8}{405 r} + \frac{32 p_{r_*}^5 v_0^{10}}{135} - \frac{64 p_{r_*}^3}{135 r^{13} v_0^{14}} - \frac{32 p_{r_*}^3}{27 r^{10} v_0^8} - \frac{904 p_{r_*}^3}{135 r^7 v_0^2} + \frac{3971393821 p_{r_*}^3}{779625 r^6} + \frac{381776 p_{r_*}^3 \ln r}{1575 r^6} + \frac{318536 p_{r_*}^3 v_0^2}{8505 r^5}$$
$$+ \frac{56}{405} p_{r_*}^3 r^4 v_0^{20} + \frac{1412 p_{r_*}^3 v_0^4}{135 r^4} + \frac{29455 p_{r_*}^3 r^3 v_0^{18}}{2772} + \frac{1662031157 p_{r_*}^3 v_0^6}{1039500 r^3} - \frac{54784 p_{r_*}^3 v_0^6 \ln r}{175 r^3} + \frac{68168 p_{r_*}^3 v_0^8}{8505 r^2}$$
$$+ \frac{8}{63} p_{r_*}^3 r^2 v_0^{16} - \frac{496 p_{r_*}^3 v_0^{10}}{315 r} - \frac{244}{405} p_{r_*}^3 r v_0^{14} - \frac{4446151 p_{r_*}^3 v_0^{12}}{27720} - \frac{128 p_{r_*}}{405 r^{14} v_0^{14}} - \frac{32 p_{r_*}}{45 r^{11} v_0^8} - \frac{448 p_{r_*}}{135 r^8 v_0^2} + \frac{16}{405} p_{r_*} r^6 v_0^{26}$$
$$+ \frac{2392124741 p_{r_*}}{779625 r^7} + \frac{398896 p_{r_*} \ln r}{1575 r^7} + \frac{126944 p_{r_*} v_0^2}{1701 r^6} - \frac{1871}{990} p_{r_*} r^5 v_0^{24} + \frac{458 p_{r_*} r^4 v_0^{22}}{2835} - \frac{1686962227 p_{r_*} v_0^6}{1559250 r^4}$$
$$- \frac{75328 p_{r_*} v_0^6 \ln r}{225 r^4} - \frac{17}{15} p_{r_*} r^3 v_0^{20} - \frac{166324 p_{r_*} v_0^8}{2835 r^3} - \frac{41657 p_{r_*} r^2 v_0^{18}}{8100} + \frac{560238598 p_{r_*} v_0^{10}}{779625 r^2} + \frac{109568 p_{r_*} v_0^{10} \ln v_0}{525 r^2}$$
$$+ \frac{54784 p_{r_*} v_0^{10} \ln 2}{525 r^2} - \frac{38}{45} p_{r_*} r v_0^{16} - \frac{320493581 p_{r_*} v_0^{12}}{115500 r} + \frac{32528 p_{r_*} v_0^{12} \ln r}{175 r} + \frac{25276 p_{r_*} v_0^{14}}{1701} \ , \tag{A10h}$$

$$\mathcal{F}_r^{\text{3PN, Tail}} = -\frac{89498224 p_{r_*}^5}{7875 r^5} + \frac{208984375 p_{r_*}^5 \ln 5}{378 r^5} + \frac{1061386821 p_{r_*}^5 \ln 3}{1750 r^5} - \frac{17548301312 p_{r_*}^5 \ln 2}{7875 r^5} + \frac{7482724 p_{r_*}^5 v_0^6}{2625 r^2}$$
$$- \frac{41796875 p_{r_*}^5 v_0^6 \ln 5}{189 r^2} - \frac{34399323 p_{r_*}^5 v_0^6 \ln 3}{125 r^2} + \frac{22339490816 p_{r_*}^5 v_0^6 \ln 2}{23625 r^2} - \frac{11248 \pi^2 p_{r_*}^3}{45 r^6} + \frac{1203536 \gamma p_{r_*}^3}{1575 r^6}$$
$$- \frac{100258619 p_{r_*}^3}{18375 r^6} - \frac{601768 p_{r_*}^3 \ln r}{525 r^6} - \frac{3588138 p_{r_*}^3 \ln 3}{35 r^6} + \frac{828630256 p_{r_*}^3 \ln 2}{4725 r^6} + \frac{1550216 p_{r_*}^3 v_0^6}{525 r^3} - \frac{6608 \pi^2 p_{r_*}}{45 r^7}$$
$$+ \frac{1872072 p_{r_*}^3 v_0^6 \ln 3}{35 r^3} - \frac{140575744 p_{r_*}^3 v_0^6 \ln 2}{1575 r^3} + \frac{101008 \gamma p_{r_*}}{225 r^7} + \frac{109379 p_{r_*}}{7875 r^7} - \frac{50504 p_{r_*} \ln r}{75 r^7} + \frac{468018 p_{r_*} \ln 3}{175 r^7}$$
$$- \frac{2826512 p_{r_*} \ln 2}{1575 r^7} + \frac{5072 \pi^2 p_{r_*} v_0^6}{45 r^4} - \frac{542704 \gamma p_{r_*} v_0^6}{1575 r^4} + \frac{10443403 p_{r_*} v_0^6}{55125 r^4} + \frac{271352 p_{r_*} v_0^6 \ln r}{525 r^4} + \frac{512 \pi^2 p_{r_*} v_0^{10}}{15 r^2}$$
$$- \frac{468018 p_{r_*} v_0^6 \ln 3}{175 r^4} + \frac{3155216 p_{r_*} v_0^6 \ln 2}{1575 r^4} - \frac{54784 \gamma p_{r_*} v_0^{10}}{525 r^2} - \frac{2777632 p_{r_*} v_0^{10}}{18375 r^2} - \frac{54784 p_{r_*} v_0^{10} \ln v_0}{175 r^2}$$
$$- \frac{54784 p_{r_*} v_0^{10} \ln 2}{175 r^2} \ . \tag{A10i}$$

The azimuthal component is

$$\mathcal{F}_\varphi^{\text{ecc,add}} = \mathcal{F}_\varphi^{\text{0PN}} + \mathcal{F}_\varphi^{\text{1PN}} + \mathcal{F}_\varphi^{\text{1.5PN,Tail}} + \mathcal{F}_\varphi^{\text{1.5PN,SO}} + \mathcal{F}_\varphi^{\text{2PN}} + \mathcal{F}_\varphi^{\text{2PN,SS}} + \mathcal{F}_\varphi^{\text{2.5PN,Tail}} + \mathcal{F}_\varphi^{\text{3PN}} + \mathcal{F}_\varphi^{\text{3PN,Tail}} \ , \tag{A11}$$

while all the different PN orders are given by

$$\mathcal{F}_\varphi^{\text{0PN}} = -\frac{232 p_{r_*}^2 v_0^3}{15 r} - \frac{176 v_0^3}{15 r^2} + \frac{16 r v_0^9}{3} + \frac{32 v_0^7}{5} \ , \tag{A12a}$$

$$\mathcal{F}_\varphi^{\text{1PN}} = \frac{58 p_{r_*}^4}{15 r^4 v_0^3} - \frac{58 p_{r_*}^4 v_0^3}{105 r} + \frac{32 p_{r_*}^2}{3 r^5 v_0^3} - \frac{56 p_{r_*}^2 v_0}{15 r^3} + \frac{5497 p_{r_*}^2 v_0^3}{105 r^2} + \frac{374}{105} p_{r_*}^2 r v_0^9 + \frac{8 p_{r_*}^2 v_0^7}{3} + \frac{88}{15 r^6 v_0^3}$$

$$+ \frac{8r^4 v_0^{17}}{45} - \frac{112 v_0}{15 r^4} - \frac{46 r^3 v_0^{15}}{35} + \frac{3217 v_0^3}{105 r^3} + \frac{8 r^2 v_0^{13}}{3} - \frac{8 v_0^7}{5r} - \frac{1825 v_0^9}{63} \ , \tag{A12b}$$

$$\mathcal{F}_\varphi^{1.5\mathrm{PN,Tail}} = \pi \left[\frac{49 p_{r_*}^6}{225 r^2} - \frac{342 p_{r_*}^2}{5 r^4} - \frac{334}{15 r^5} - \frac{10 v_0^6}{3 r^2} + \frac{128 v_0^{10}}{5} \right] , \tag{A12c}$$

$$\mathcal{F}_\varphi^{1.5\mathrm{PN,SO}} = a \left[\frac{16 p_{r_*}^4}{r^3} + \frac{88 p_{r_*}^2}{r^4} + \frac{48 p_{r_*}^2 v_0^6}{5r} + \frac{176}{5 r^5} - \frac{8}{15} r^4 v_0^{18} - \frac{224 v_0^4}{15 r^3} - \frac{4 v_0^6}{15 r^2} - \frac{12}{5} r v_0^{12} - \frac{256 v_0^{10}}{15} \right] , \tag{A12d}$$

$$\mathcal{F}_\varphi^{2\mathrm{PN}} = \frac{29 p_{r_*}^6}{60 r^7 v_0^9} - \frac{58 p_{r_*}^6}{21 r^4 v_0^3} + \frac{2699 p_{r_*}^6 v_0^3}{1260 r} + \frac{23 p_{r_*}^4}{10 r^8 v_0^9} + \frac{7 p_{r_*}^4}{45 r^6 v_0^5} - \frac{4891 p_{r_*}^4}{420 r^5 v_0^3} + \frac{56 p_{r_*}^4 v_0}{45 r^3} + \frac{453 p_{r_*}^4 v_0^3}{140 r^2} - \frac{152}{21} p_{r_*}^4 r v_0^9$$
$$- \frac{7 p_{r_*}^4 v_0^7}{9} + \frac{17 p_{r_*}^2}{5 r^9 v_0^9} + \frac{28 p_{r_*}^2}{45 r^7 v_0^5} - \frac{813 p_{r_*}^2}{28 r^6 v_0^3} - \frac{2}{27} p_{r_*}^2 r^4 v_0^{17} - \frac{266 p_{r_*}^2 v_0}{45 r^4} + \frac{2591}{420} p_{r_*}^2 r^3 v_0^{15} + \frac{78314 p_{r_*}^2 v_0^3}{189 r^3}$$
$$- \frac{2}{9} p_{r_*}^2 r^2 v_0^{13} - \frac{34}{135} p_{r_*}^2 r v_0^{11} + \frac{248 p_{r_*}^2 v_0^7}{45 r} - \frac{2104 p_{r_*}^2 v_0^9}{35} + \frac{22}{15 r^{10} v_0^9} + \frac{28}{45 r^8 v_0^5} - \frac{1007}{70 r^7 v_0^3} - \frac{2}{27} r^6 v_0^{23}$$
$$- \frac{562 r^5 v_0^{21}}{315} - \frac{28 v_0}{15 r^5} + \frac{11 r^4 v_0^{19}}{35} + \frac{1209829 v_0^3}{11340 r^4} + \frac{10 r^3 v_0^{17}}{9} + \frac{4027 r^2 v_0^{15}}{1260} - \frac{113 v_0^7}{45 r^2} + \frac{48 r v_0^{13}}{5} - \frac{12449 v_0^9}{270 r}$$
$$- \frac{31904 v_0^{11}}{567} \ , \tag{A12e}$$

$$\mathcal{F}_\varphi^{2\mathrm{PN,SS}} = a^2 \left[\frac{116 p_{r_*}^4}{15 r^5 v_0^3} + \frac{88 p_{r_*}^2}{15 r^6 v_0^3} - \frac{112 p_{r_*}^2 v_0}{15 r^4} - \frac{220 p_{r_*}^2 v_0^3}{3 r^3} + \frac{2}{5} r^4 v_0^{19} - \frac{409 v_0^3}{15 r^4} + \frac{211 v_0^9}{15 r} + \frac{64 v_0^{11}}{5} \right] , \tag{A12f}$$

$$\mathcal{F}_\varphi^{2.5\mathrm{PN,Tail}} = \pi \left[\frac{12083 p_{r_*}^6}{3780 r^3} - \frac{267293 p_{r_*}^4}{2520 r^4} - \frac{10403 p_{r_*}^2}{35 r^5} - \frac{64 p_{r_*}^2 v_0^4}{3 r^3} - \frac{5 p_{r_*}^2 v_0^6}{r^2} + \frac{64}{15} p_{r_*}^2 v_0^{10} - \frac{2039}{70 r^6} + \frac{16}{45} r^4 v_0^{20} \right.$$
$$\left. - \frac{128 v_0^4}{3 r^4} + \frac{22499 v_0^6}{210 r^3} + \frac{64}{15} r^2 v_0^{16} + \frac{64 v_0^{10}}{5r} - \frac{16621 v_0^{12}}{315} \right] , \tag{A12g}$$

$$\mathcal{F}_\varphi^{3\mathrm{PN}} = \frac{5 r^8 v_0^{29}}{324} - \frac{1433 r^7 v_0^{27}}{6160} + \frac{173 r^6 v_0^{25}}{1620} + \frac{11}{162} p_{r_*}^2 r^6 v_0^{23} - \frac{89 r^5 v_0^{23}}{135} + \frac{1009 p_{r_*}^2 r^5 v_0^{21}}{18480} - \frac{65599427 r^4 v_0^{21}}{4989600}$$
$$- \frac{11}{60} p_{r_*}^2 r^4 v_0^{19} + \frac{3583 r^3 v_0^{19}}{1260} + \frac{17}{324} p_{r_*}^4 r^4 v_0^{17} - \frac{88}{405} p_{r_*}^2 r^3 v_0^{17} + \frac{18203 r^2 v_0^{17}}{34020} - \frac{30493 p_{r_*}^4 r^3 v_0^{15}}{3080}$$
$$+ \frac{209245 p_{r_*}^2 r^2 v_0^{15}}{7392} - \frac{306672181 r v_0^{15}}{1188000} + \frac{6848}{175} r v_0^{15} \ln r + \frac{13}{108} p_{r_*}^4 r^2 v_0^{13} + \frac{269 p_{r_*}^2 r v_0^{13}}{1260} + \frac{109568}{525} v_0^{13} \ln v_0$$
$$+ \frac{54784 \ln 2}{525} v_0^{13} + \frac{2290065817 v_0^{13}}{3118500} - \frac{21307 p_{r_*}^2 v_0^{11}}{3402} + \frac{119}{405} p_{r_*}^4 r v_0^{11} - \frac{42736 v_0^{11}}{945 r} + \frac{236999 p_{r_*}^4 v_0^9}{3168}$$
$$+ \frac{27463 p_{r_*}^6 r v_0^9}{2640} - \frac{46224 p_{r_*}^2 v_0^9 \ln r}{175 r} + \frac{1712 v_0^9 \ln r}{63 r^2} + \frac{45309763 p_{r_*}^2 v_0^9}{23625 r} - \frac{49307783 v_0^9}{79200 r^2} + \frac{133 p_{r_*}^6 v_0^7}{324}$$
$$- \frac{1451 p_{r_*}^4 v_0^7}{540 r} + \frac{7427 p_{r_*}^2 v_0^7}{540 r^2} - \frac{2269 v_0^7}{180 r^3} + \frac{187 p_{r_*}^4 v_0^5}{1620 r^2} + \frac{87736 p_{r_*}^2 v_0^5}{1701 r^3} + \frac{873433 v_0^5}{8505 r^4} + \frac{6848 p_{r_*}^4 v_0^3 \ln r}{175 r^3}$$
$$+ \frac{232832 p_{r_*}^2 v_0^3 \ln r}{1575 r^4} + \frac{1712 v_0^3 \ln r}{45 r^5} - \frac{49153 p_{r_*}^8 v_0^3}{18480 r} - \frac{1878557 p_{r_*}^6 v_0^3}{184800 r^2} - \frac{3763348417 p_{r_*}^4 v_0^3}{8316000 r^3}$$
$$+ \frac{2982393643 p_{r_*}^2 v_0^3}{8316000 r^4} + \frac{189547637 v_0^3}{1663200 r^5} - \frac{77 p_{r_*}^6 v_0}{108 r^3} + \frac{539 p_{r_*}^4 v_0}{180 r^4} - \frac{7861 p_{r_*}^2 v_0}{540 r^5} - \frac{175 v_0}{54 r^6} + \frac{8959 p_{r_*}^8}{5040 r^4 v_0^3}$$
$$+ \frac{1169 p_{r_*}^6}{720 r^5 v_0^3} - \frac{480959 p_{r_*}^4}{4320 r^6 v_0^3} - \frac{10877563 p_{r_*}^2}{45360 r^7 v_0^3} - \frac{279001}{5670 r^8 v_0^3} - \frac{91 p_{r_*}^6}{540 r^6 v_0^5} + \frac{7 p_{r_*}^4}{108 r^7 v_0^5} + \frac{28 p_{r_*}^2}{27 r^8 v_0^5} + \frac{7}{15 r^9 v_0^5}$$
$$- \frac{1189 p_{r_*}^8}{1680 r^7 v_0^9} - \frac{9017 p_{r_*}^6}{3360 r^8 v_0^9} - \frac{6047 p_{r_*}^4}{1120 r^9 v_0^9} - \frac{3041 p_{r_*}^2}{420 r^{10} v_0^9} - \frac{509}{168 r^{11} v_0^9} + \frac{7 p_{r_*}^6}{324 r^9 v_0^{11}} + \frac{7 p_{r_*}^4}{54 r^{10} v_0^{11}} + \frac{7 p_{r_*}^2}{27 r^{11} v_0^{11}}$$

$$+ \frac{14}{81r^{12}v_0^{11}} + \frac{29p_{r_*}^8}{240r^{10}v_0^{15}} + \frac{49p_{r_*}^6}{60r^{11}v_0^{15}} + \frac{2p_{r_*}^4}{r^{12}v_0^{15}} + \frac{31p_{r_*}^2}{15r^{13}v_0^{15}} + \frac{11}{15r^{14}v_0^{15}} \ , \tag{A12h}$$

$$\begin{aligned}
\mathcal{F}_\varphi^{\text{3PN,Tail}} = & -\frac{7482724p_{r_*}^6 v_0^3}{2625r^2} + \frac{41796875p_{r_*}^6 v_0^3 \ln 5}{189r^2} + \frac{34399323p_{r_*}^6 v_0^3 \ln 3}{125r^2} - \frac{22339490816p_{r_*}^6 v_0^3 \ln 2}{23625r^2} - \frac{1550216p_{r_*}^4 v_0^3}{525r^3} \\
& - \frac{1872072p_{r_*}^4 v_0^3 \ln 3}{35r^3} + \frac{140575744p_{r_*}^4 v_0^3 \ln 2}{1575r^3} + \frac{1136\pi^2 p_{r_*}^2 v_0^3}{45r^4} - \frac{121552\gamma p_{r_*}^2 v_0^3}{1575r^4} - \frac{29951111p_{r_*}^2 v_0^3}{55125r^4} + \frac{16\pi^2 v_0^3}{45r^5} \\
& + \frac{60776p_{r_*}^2 v_0^3 \ln r}{525r^4} - \frac{156006p_{r_*}^2 v_0^3 \ln 3}{175r^4} + \frac{1111088p_{r_*}^2 v_0^3 \ln 2}{1575r^4} - \frac{1712\gamma v_0^3}{1575r^5} + \frac{8511719v_0^3}{55125r^5} + \frac{856v_0^3 \ln r}{525r^5} \\
& - \frac{156006v_0^3 \ln 3}{175r^5} + \frac{279056v_0^3 \ln 2}{315r^5} - \frac{1552\pi^2 v_0^9}{45r^2} + \frac{166064\gamma v_0^9}{1575r^2} + \frac{2697337v_0^9}{55125r^2} - \frac{83032v_0^9 \ln r}{525r^2} + \frac{156006v_0^9 \ln 3}{175r^2} \\
& - \frac{152368v_0^9 \ln 2}{225r^2} + \frac{512\pi^2 v_0^{13}}{15} - \frac{54784\gamma v_0^{13}}{525} - \frac{2777632v_0^{13}}{18375} - \frac{54784}{175}v_0^{13} \ln v_0 - \frac{54784 \ln 2}{175}v_0^{13} \ , \tag{A12i}
\end{aligned}$$

3. Schott terms

Here we provide the expressions of the total time derivative of the Schott terms introduced in equations (18a) and (18b). They are expressed as functions of the variables $\{r, p_{r_*}, v_0\}$. For the Schott term contribution to the energy balance equation we have

$$\dot{E}_{\text{Schott}} = \dot{E}_{\text{Sch}}^{\text{0PN}} + \dot{E}_{\text{Sch}}^{\text{1PN}} + \dot{E}_{\text{Sch}}^{\text{1.5PN,Tail}} + \dot{E}_{\text{Sch}}^{\text{1.5PN,SO}} + \dot{E}_{\text{Sch}}^{\text{2PN}} + \dot{E}_{\text{Sch}}^{\text{2PN,SS}} + \dot{E}_{\text{Sch}}^{\text{2.5PN,Tail}} + \dot{E}_{\text{Sch}}^{\text{3PN}} + \dot{E}_{\text{Sch}}^{\text{3PN,Tail}} \ , \tag{A13}$$

where

$$\dot{E}_{\text{Sch}}^{\text{0PN}} = -\frac{152p_{r_*}^4}{15r^3} - \frac{76p_{r_*}^2}{5r^4} + \frac{548p_{r_*}^2 v_0^6}{15r} + \frac{16v_0^6}{3r^2} - \frac{16rv_0^{12}}{3} \ , \tag{A14a}$$

$$\dot{E}_{\text{Sch}}^{\text{1PN}} = -\frac{584p_{r_*}^6}{105r^3} - \frac{20213p_{r_*}^4}{105r^4} - \frac{1142p_{r_*}^4 v_0^6}{105r} - \frac{4003p_{r_*}^2}{21r^5} + \frac{12794p_{r_*}^2 v_0^6}{105r^2} - \frac{8}{3}p_{r_*}^2 rv_0^{12} - \frac{592}{105r^6} + \frac{278r^3 v_0^{18}}{105} + \frac{215v_0^6}{21r^3} - \frac{761v_0^{12}}{105} \ , \tag{A14b}$$

$$\dot{E}_{\text{Sch}}^{\text{1.5PN,Tail}} = -\frac{50\pi p_{r_*}^2 v_0^3}{3r^4} - \frac{10\pi v_0^3}{3r^5} + \frac{10\pi v_0^9}{3r^2} \ , \tag{A14c}$$

$$\dot{E}_{\text{Sch}}^{\text{1.5PN,SO}} = a\left[-\frac{48p_{r_*}^4 v_0^3}{5r^3} - \frac{1708p_{r_*}^2 v_0^3}{15r^4} - \frac{36p_{r_*}^2 v_0^9}{5r} - \frac{416v_0^3}{15r^5} + \frac{76v_0^9}{3r^2} + \frac{12}{5}rv_0^{15} \right] \ , \tag{A14d}$$

$$\begin{aligned}
\dot{E}_{\text{Sch}}^{\text{2PN}} = & \frac{2593p_{r_*}^8}{315r^3} + \frac{5633p_{r_*}^6}{45r^4} + \frac{5368p_{r_*}^6 v_0^6}{315r} - \frac{224522p_{r_*}^4}{189r^5} + \frac{70018p_{r_*}^4 v_0^6}{315r^2} + \frac{199}{21}p_{r_*}^4 rv_0^{12} - \frac{1864133p_{r_*}^2}{1890r^6} + \frac{88}{45}p_{r_*}^2 r^3 v_0^{18} \\
& + \frac{7235p_{r_*}^2 v_0^6}{18r^3} + \frac{25583p_{r_*}^2 v_0^{12}}{315} - \frac{967}{189r^7} + \frac{58r^5 v_0^{24}}{45} - \frac{161113v_0^6}{1890r^4} - \frac{388r^2 v_0^{18}}{35} + \frac{189299v_0^{12}}{1890r} \ , \tag{A14e}
\end{aligned}$$

$$\dot{E}_{\text{Sch}}^{\text{2PN, SS}} = a^2\left[-\frac{268p_{r_*}^4}{15r^5} + \frac{73p_{r_*}^2}{15r^6} + \frac{1193p_{r_*}^2 v_0^6}{15r^3} + \frac{211v_0^6}{15r^4} - \frac{211v_0^{12}}{15r} \right] \ , \tag{A14f}$$

$$\dot{E}_{\text{Sch}}^{\text{2.5PN, Tail}} = \pi\left[\frac{25p_{r_*}^4}{6r^7 v_0^3} + \frac{25p_{r_*}^4 v_0^3}{2r^4} + \frac{55p_{r_*}^2}{6r^8 v_0^3} + \frac{153397p_{r_*}^2 v_0^3}{210r^5} + \frac{35p_{r_*}^2 v_0^9}{3r^2} + \frac{5}{3r^9 v_0^3} + \frac{4052v_0^3}{35r^6} - \frac{24487v_0^9}{210r^3} - \frac{5v_0^{15}}{6} \right] \ , \tag{A14g}$$

$$\begin{aligned}
\dot{E}_{\text{Sch}}^{\text{3PN}} = & -\frac{3277p_{r_*}^{10}}{385r^3} - \frac{442027p_{r_*}^8}{6930r^4} - \frac{130111p_{r_*}^8 v_0^6}{6930r} - \frac{272717041p_{r_*}^6}{1039500r^5} + \frac{27392p_{r_*}^6 \ln r}{175r^5} - \frac{1662869p_{r_*}^6 v_0^6}{13860r^2} - \frac{41786p_{r_*}^6 rv_0^{12}}{3465} \\
& - \frac{42507545p_{r_*}^4}{16632r^6} - \frac{80464p_{r_*}^4 \ln r}{315r^6} - \frac{146}{55}p_{r_*}^4 r^3 v_0^{18} - \frac{1432689791p_{r_*}^4 v_0^6}{2079000r^3} + \frac{6848p_{r_*}^4 v_0^6 \ln r}{25r^3} - \frac{109225p_{r_*}^4 v_0^{12}}{1386}
\end{aligned}$$

$$- \frac{34926373 p_{r_*}^2}{31500 r^7} - \frac{142096 p_{r_*}^2 \ln r}{525 r^7} - \frac{3716 p_{r_*}^2 r^5 v_0^{24}}{3465} + \frac{3100400579 p_{r_*}^2 v_0^6}{1039500 r^4} - \frac{198592 p_{r_*}^2 v_0^6 \ln r}{1575 r^4} - \frac{321193 p_{r_*}^2 r^2 v_0^{18}}{13860}$$

$$- \frac{127528781 p_{r_*}^2 v_0^{12}}{346500 r} + \frac{13696 p_{r_*}^2 v_0^{12} \ln r}{175 r} + \frac{880568}{10395 r^8} - \frac{1483 r^7 v_0^{30}}{6930} + \frac{7537561 v_0^6}{38500 r^5} - \frac{142096 v_0^6 \ln r}{1575 r^5} + \frac{1417 r^4 v_0^{24}}{770}$$

$$- \frac{1133672317 v_0^{12}}{2079000 r^2} + \frac{29104 v_0^{12} \ln r}{225 r^2} + \frac{182383141 r v_0^{18}}{693000} - \frac{6848}{175} r v_0^{18} \ln r \ , \tag{A14h}$$

$$\dot{E}_{\mathrm{Sch}}^{\mathrm{3PN, \, Tail}} = - \frac{1552 \pi^2 p_{r_*}^4}{9 r^6} + \frac{166064 \gamma p_{r_*}^4}{315 r^6} + \frac{4441009 p_{r_*}^4}{11025 r^6} - \frac{83032 p_{r_*}^4 \ln r}{105 r^6} + \frac{156006 p_{r_*}^4 \ln 3}{35 r^6} - \frac{152368 p_{r_*}^4 \ln 2}{45 r^6}$$

$$- \frac{4624 \pi^2 p_{r_*}^2}{15 r^7} + \frac{494768 \gamma p_{r_*}^2}{525 r^7} + \frac{27991609 p_{r_*}^2}{18375 r^7} - \frac{247384 p_{r_*}^2 \ln r}{175 r^7} + \frac{468018 p_{r_*}^2 \ln 3}{175 r^7} - \frac{409168 p_{r_*}^2 \ln 2}{525 r^7}$$

$$- \frac{6208 \pi^2 p_{r_*}^2 v_0^6}{45 r^4} + \frac{664256 \gamma p_{r_*}^2 v_0^6}{1575 r^4} + \frac{19507708 p_{r_*}^2 v_0^6}{55125 r^4} - \frac{332128 p_{r_*}^2 v_0^6 \ln r}{525 r^4} + \frac{624024 p_{r_*}^2 v_0^6 \ln 3}{175 r^4}$$

$$- \frac{609472 p_{r_*}^2 v_0^6 \ln 2}{225 r^4} - \frac{512 \pi^2}{15 r^8} + \frac{54784 \gamma}{525 r^8} + \frac{3736352}{18375 r^8} - \frac{27392 \ln r}{175 r^8} + \frac{109568 \ln 2}{525 r^8} - \frac{16 \pi^2 v_0^6}{45 r^5} + \frac{1712 \gamma v_0^6}{1575 r^5}$$

$$- \frac{8511719 v_0^6}{55125 r^5} - \frac{856 v_0^6 \ln r}{525 r^5} + \frac{156006 v_0^6 \ln 3}{175 r^5} - \frac{279056 v_0^6 \ln 2}{315 r^5} + \frac{1552 \pi^2 v_0^{12}}{45 r^2} - \frac{166064 \gamma v_0^{12}}{1575 r^2} - \frac{2697337 v_0^{12}}{55125 r^2}$$

$$+ \frac{83032 v_0^{12} \ln r}{525 r^2} - \frac{156006 v_0^{12} \ln 3}{175 r^2} + \frac{152368 v_0^{12} \ln 2}{225 r^2} \ , \tag{A14i}$$

while for the Schott terms related to the angular momentum flux we have

$$\dot{J}_{\mathrm{Schott}} = \dot{j}_{\mathrm{Sch}}^{\mathrm{0PN}} + \dot{j}_{\mathrm{Sch}}^{\mathrm{1PN}} + \dot{j}_{\mathrm{Sch}}^{\mathrm{1.5PN, Tail}} + \dot{j}_{\mathrm{Sch}}^{\mathrm{1.5PN, SO}} + \dot{j}_{\mathrm{Sch}}^{\mathrm{2PN}} + \dot{j}_{\mathrm{Sch}}^{\mathrm{2PN, SS}} + \dot{j}_{\mathrm{Sch}}^{\mathrm{2.5PN, Tail}} + \dot{j}_{\mathrm{Sch}}^{\mathrm{3PN}} + \dot{j}_{\mathrm{Sch}}^{\mathrm{3PN, Tail}} \ , \tag{A15}$$

with

$$\dot{j}_{\mathrm{Sch}}^{\mathrm{0PN}} = \frac{256 p_{r_*}^2 v_0^3}{15 r} + \frac{128 v_0^3}{15 r^2} - \frac{128 r v_0^9}{15} \ , \tag{A16a}$$

$$\dot{j}_{\mathrm{Sch}}^{\mathrm{1PN}} = - \frac{64 p_{r_*}^4}{15 r^4 v_0^3} - \frac{64 p_{r_*}^4 v_0^3}{15 r} - \frac{32 p_{r_*}^2}{3 r^5 v_0^3} - \frac{6227 p_{r_*}^2 v_0^3}{105 r^2} - \frac{32}{5} p_{r_*}^2 r v_0^9 - \frac{64}{15 r^6 v_0^3} - \frac{32}{15} r^3 v_0^{15} - \frac{219 v_0^3}{35 r^3} + \frac{443 v_0^9}{35} \ , \tag{A16b}$$

$$\dot{j}_{\mathrm{Sch}}^{\mathrm{1.5PN, Tail}} = - \frac{10 \pi p_{r_*}^2}{r^4} - \frac{10 \pi}{3 r^5} + \frac{10 \pi v_0^6}{3 r^2} \ , \tag{A16c}$$

$$\dot{j}_{\mathrm{Sch}}^{\mathrm{1.5PN, SO}} = a \left[- \frac{16 p_{r_*}^4}{r^3} - \frac{448 p_{r_*}^2}{5 r^4} - \frac{24 p_{r_*}^2 v_0^6}{5 r} - \frac{152}{5 r^5} + \frac{116 v_0^6}{5 r^2} + \frac{36}{5} r v_0^{12} \right] , \tag{A16d}$$

$$\dot{j}_{\mathrm{Sch}}^{\mathrm{2PN}} = - \frac{8 p_{r_*}^6}{15 r^7 v_0^9} + \frac{64 p_{r_*}^6}{15 r^4 v_0^3} + \frac{8 p_{r_*}^6 v_0^3}{3 r} - \frac{12 p_{r_*}^4}{5 r^8 v_0^9} + \frac{2113 p_{r_*}^4}{140 r^5 v_0^3} + \frac{5443 p_{r_*}^4 v_0^3}{420 r^2} + 4 p_{r_*}^4 r v_0^9 - \frac{16 p_{r_*}^2}{5 r^9 v_0^9} + \frac{1681 p_{r_*}^2}{60 r^6 v_0^3} + \frac{16}{15} p_{r_*}^2 r^3 v_0^{15} \tag{A16e}$$

$$- \frac{1487299 p_{r_*}^2 v_0^3}{3780 r^3} - \frac{71 p_{r_*}^2 v_0^9}{105} - \frac{16}{15 r^{10} v_0^9} + \frac{881}{210 r^7 v_0^3} - \frac{4}{15} r^5 v_0^{21} - \frac{84881 v_0^3}{756 r^4} - \frac{2143 r^2 v_0^{15}}{420} + \frac{216437 v_0^9}{1890 r} \ , \tag{A16f}$$

$$\dot{j}_{\mathrm{Sch}}^{\mathrm{2PN, SS}} = a^2 \left[- \frac{128 p_{r_*}^4}{15 r^5 v_0^3} - \frac{64 p_{r_*}^2}{15 r^6 v_0^3} + \frac{1292 p_{r_*}^2 v_0^3}{15 r^3} + \frac{307 v_0^3}{15 r^4} - \frac{307 v_0^9}{15 r} \right] , \tag{A16g}$$

$$\dot{j}_{\mathrm{Sch}}^{\mathrm{2.5PN, Tail}} = \pi \left[\frac{5 p_{r_*}^4}{r^4} + \frac{46048 p_{r_*}^2}{105 r^5} + \frac{5 p_{r_*}^2 v_0^6}{r^2} + \frac{22499}{210 r^6} - \frac{22499 v_0^6}{210 r^3} \right] , \tag{A16h}$$

$$\dot{j}_{\mathrm{Sch}}^{\mathrm{3PN}} = - \frac{2 p_{r_*}^8}{15 r^{10} v_0^{15}} + \frac{14 p_{r_*}^8}{15 r^7 v_0^9} - \frac{62 p_{r_*}^8}{15 r^4 v_0^3} - \frac{2 p_{r_*}^8 v_0^3}{r} - \frac{13 p_{r_*}^6}{15 r^{11} v_0^{15}} + \frac{11603 p_{r_*}^6}{3360 r^8 v_0^9} - \frac{2923 p_{r_*}^6}{420 r^5 v_0^3} - \frac{27551 p_{r_*}^6 v_0^3}{3360 r^2} - \frac{49}{15} p_{r_*}^6 r v_0^9$$
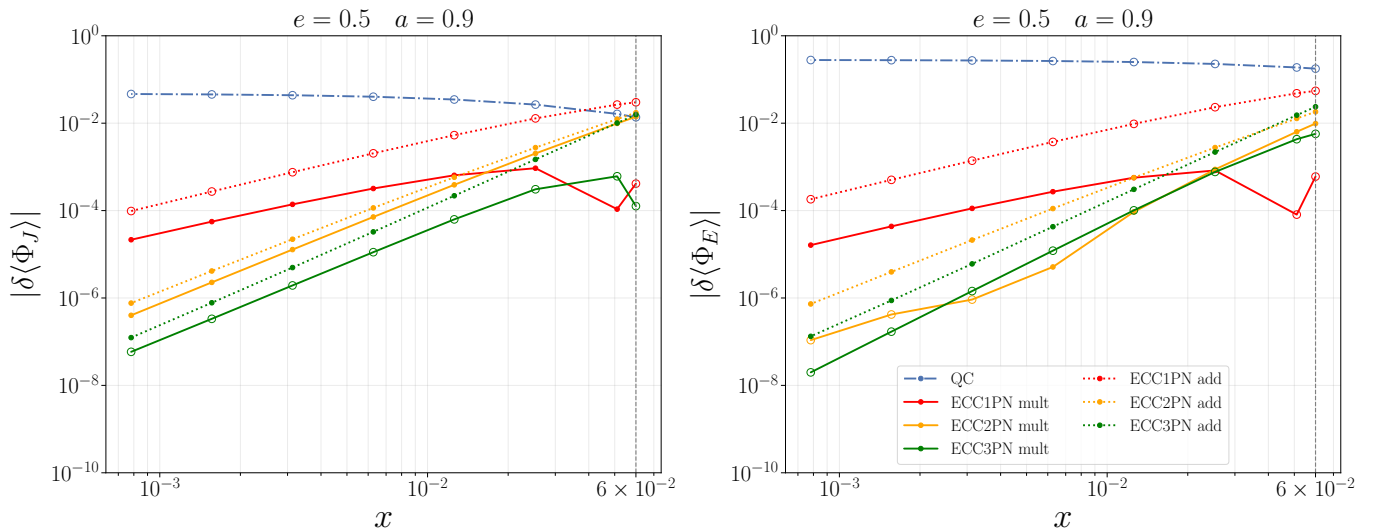
FIG. 7. Absolute value of the fractional differences defined in Eq. (22) of the averaged fluxes computed on orbits in a weak-field regime. The x-axis corresponds to the gauge-invariant variable $x = \langle \dot{\varphi} \rangle^{2/3}$. The orbits are characterized by the parameters $e = 0.5$, $a = 0.9$ and $p = \{960, 480, 240, 120, 60, 30, 15, 12.797\}$. Dotted lines correspond to the additive implementation (add) while solid lines correspond to the multiplicative (mult) implementation. Empty circle dots represent negative values of the fractional differences, highlighting zero crossing in the log-log plots. We highlight with a dashed vertical gray line the orbit with $x = 0.06$, which is also shown in the contour plot of Fig. 4.

$$
\begin{aligned}
&- \frac{2p_{r_*}^4}{r^{12}v_0^{15}} + \frac{20189p_{r_*}^4}{3360r^9v_0^9} + \frac{3187889p_{r_*}^4}{30240r^6v_0^3} - p_{r_*}^4 r^3 v_0^{15} + \frac{481217p_{r_*}^4 v_0^3}{4320r^3} + \frac{399p_{r_*}^4 v_0^9}{160} - \frac{28p_{r_*}^2}{15r^{13}v_0^{15}} + \frac{1273p_{r_*}^2}{210r^{10}v_0^9} \\
&+ \frac{56683p_{r_*}^2}{240r^7v_0^3} + \frac{1}{3}p_{r_*}^2 r^5 v_0^{21} + \frac{675397039p_{r_*}^2 v_0^3}{1663200r^4} - \frac{70192p_{r_*}^2 v_0^3 \ln r}{315r^4} + \frac{2713p_{r_*}^2 r^2 v_0^{15}}{1120} + \frac{2011469p_{r_*}^2 v_0^9}{15120r} - \frac{8}{15r^{14}v_0^{15}} \\
&+ \frac{219}{280r^{11}v_0^9} + \frac{102103}{1890r^8v_0^3} + \frac{r^7v_0^{27}}{15} - \frac{121954519v_0^3}{1188000r^5} - \frac{70192v_0^3 \ln r}{1575r^5} - \frac{449r^4v_0^{21}}{224} + \frac{302957833v_0^9}{8316000r^2} + \frac{70192v_0^9 \ln r}{1575r^2} \\
&+ \frac{420059rv_0^{15}}{30240} \,,
\end{aligned}
\tag{A16i}
$$

$$
\begin{aligned}
\dot{J}_{\mathrm{Sch}}^{\mathrm{3PN, \, Tail}} = &- \frac{1552\pi^2 p_{r_*}^2 v_0^3}{9r^4} + \frac{166064\gamma p_{r_*}^2 v_0^3}{315r^4} + \frac{4441009p_{r_*}^2 v_0^3}{11025r^4} - \frac{83032p_{r_*}^2 v_0^3 \ln r}{105r^4} + \frac{156006p_{r_*}^2 v_0^3 \ln 3}{35r^4} - \frac{1552\pi^2 v_0^3}{45r^5} \\
&- \frac{152368p_{r_*}^2 v_0^3 \ln 2}{45r^4} + \frac{166064\gamma v_0^3}{1575r^5} + \frac{2697337v_0^3}{55125r^5} - \frac{83032v_0^3 \ln r}{525r^5} + \frac{156006v_0^3 \ln 3}{175r^5} - \frac{152368v_0^3 \ln 2}{225r^5} \\
&+ \frac{1552\pi^2 v_0^9}{45r^2} - \frac{166064\gamma v_0^9}{1575r^2} - \frac{2697337v_0^9}{55125r^2} + \frac{83032v_0^9 \ln r}{525r^2} - \frac{156006v_0^9 \ln 3}{175r^2} + \frac{152368v_0^9 \ln 2}{225r^2} .
\end{aligned}
\tag{A16j}
$$

We remark that these total time derivatives of the Schott terms have to be computed on the geodesics and plugged in the balance equations.

4. PN scaling assessment for spinning orbits

In Fig. 7, we show a similar plot to the one in Fig. 2 for eccentric orbits with $e = 0.5$ around a Kerr BH with spin $a = 0.9$. We test the weak-field regime scaling of the different PN order of the eccentric corrections to the RR force in Eq. (6) by studying the fractional differences of the orbit-averaged analytical and numerical fluxes. As in the non-spinning case, we recover the correct scaling of the different PN truncations, which is expected to be

$x^{-(n+1/2)}$, with n being the PN order at which we perform the truncation. However, in the spinning case, our analysis has an important caveat: the analytical fluxes we consider contain SO and SS spin corrections at 2PN. This means that the ECC3PN fluxes do not contain the spin contributions at 2.5PN and 3PN. As a consequence the ECC3PN lines in Fig. 7 exhibit the same scaling (slope) as the ECC2PN, but they still improve the ECC2PN lines exhibiting a shift down. In the plot we highlight with a vertical gray curve the orbit with $x = 0.06$ which

is present in the contour plot of Fig. 4. This plot extends to regimes $x \leq 0.06$ what we found in Fig. 4: the multiplicative ECC3PN corrections in Eq. (6a) perform better than the additive ECC3PN in Eq. (6a), especially for eccentric orbits with prograde spin.

Appendix B: Instantaneous fluxes from frequency domain Teukolsky solutions

The frequency domain solutions to the Teukolsky equation at future null infinity for a particle traveling on an eccentric geodesic take the form

$$\psi_4 = \sum_{lmn} Z_{lmn\,-2}S_{lm\omega_{mn}}(\cos\theta)e^{im\phi}e^{-i\omega_{mn}t}, \quad (B1)$$

where the $_{-2}S_{lm\omega_{mn}}$ spin-weighted spheroidal harmonics of weight -2, and the mode frequencies are $\omega_{mn} = m\Omega_\phi + n\Omega_r$ with Ω_ϕ and Ω_r the azimuthal and radial frequencies. To build the instantaneous fluxes using Eqs. (17) we first project the spheroidal harmonics

$_{-2}S_{lm\omega_{mn}}$ onto spherical harmonics $_{-2}Y_{lm}$ using,

$$_{-2}S_{lm\omega_{mn}}(\cos\theta)e^{im\phi} = \sum_\ell (_{-2}b_{mn})_l^\ell\,_{-2}Y_{\ell m}(\theta,\phi), \quad (B2)$$

where the coefficients $(_{-2}b_{mn})_l^\ell$ are obtained using the algorithm of Ref. [94]. This allows us to define the spin-weighted spherical harmonic coefficients of ψ_4,

$$\mathcal{Z}_{\ell mn} = \sum_l Z_{lmn}(_{-2}b_{mn})_l^\ell. \quad (B3)$$

Combining the above expressions with Eqs. (17), and applying the orthogonality relations for products of spin-weighted harmonics when integrated over the sphere, we obtain the following closed-form expressions for the instantaneous flux,

$$\Phi_E = \frac{1}{4\pi} \sum_{\ell mnn'} \frac{\mathcal{Z}_{\ell mn}\mathcal{Z}_{\ell mn'}^*}{\omega_{mn}\omega_{mn'}} e^{-i(n-n')\Omega_r t}, \text{ and} \quad (B4a)$$

$$\Phi_J = \frac{1}{4\pi} \sum_{\ell mnn'} m \frac{\mathcal{Z}_{\ell mn}\mathcal{Z}_{\ell mn'}^*}{\omega_{mn}\omega_{mn'}^2} e^{-i(n-n')\Omega_r t}. \quad (B4b)$$

[1] B. P. Abbott *et al.* (LIGO Scientific, Virgo), GWTC-1: A Gravitational-Wave Transient Catalog of Compact Binary Mergers Observed by LIGO and Virgo during the First and Second Observing Runs, Phys. Rev. X **9**, 031040 (2019), arXiv:1811.12907 [astro-ph.HE].

[2] R. Abbott *et al.* (LIGO Scientific, Virgo), GWTC-2: Compact Binary Coalescences Observed by LIGO and Virgo During the First Half of the Third Observing Run, Phys. Rev. X **11**, 021053 (2021), arXiv:2010.14527 [gr-qc].

[3] R. Abbott *et al.* (LIGO Scientific, VIRGO), GWTC-2.1: Deep Extended Catalog of Compact Binary Coalescences Observed by LIGO and Virgo During the First Half of the Third Observing Run, - (2021), arXiv:2108.01045 [gr-qc].

[4] R. Abbott *et al.* (LIGO Scientific, VIRGO, KAGRA), GWTC-3: Compact Binary Coalescences Observed by LIGO and Virgo During the Second Part of the Third Observing Run, Phys. Rev. X" (2021), arXiv:2111.03606 [gr-qc].

[5] B. P. Abbott *et al.* (KAGRA, LIGO Scientific, Virgo, VIRGO), Prospects for observing and localizing gravitational-wave transients with Advanced LIGO, Advanced Virgo and KAGRA, Living Rev. Rel. **21**, 3 (2018), arXiv:1304.0670 [gr-qc].

[6] M. Punturo *et al.*, The einstein telescope: a third-generation gravitational wave observatory, Classical and Quantum Gravity **27**, 194002 (2010).

[7] M. Evans *et al.*, A Horizon Study for Cosmic Explorer: Science, Observatories, and Community, (2021), arXiv:2109.09882 [astro-ph.IM].

[8] P. Amaro-Seoane *et al.*, Laser interferometer space antenna (2017).

[9] S. Hild *et al.*, Sensitivity Studies for Third-Generation Gravitational Wave Observatories, Class. Quant. Grav.

28, 094013 (2011), arXiv:1012.0908 [gr-qc].

[10] B. P. Abbott *et al.* (LIGO Scientific), Exploring the Sensitivity of Next Generation Gravitational Wave Detectors, Class. Quant. Grav. **34**, 044001 (2017), arXiv:1607.08697 [astro-ph.IM].

[11] S. Babak, J. Gair, A. Sesana, E. Barausse, C. F. Sopuerta, C. P. L. Berry, E. Berti, P. Amaro-Seoane, A. Petiteau, and A. Klein, Science with the space-based interferometer LISA. V: Extreme mass-ratio inspirals, Phys. Rev. D **95**, 103012 (2017), arXiv:1703.09722 [gr-qc].

[12] J. R. Gair, S. Babak, A. Sesana, P. Amaro-Seoane, E. Barausse, C. P. L. Berry, E. Berti, and C. Sopuerta, Prospects for observing extreme-mass-ratio inspirals with LISA, J. Phys. Conf. Ser. **840**, 012021 (2017), arXiv:1704.00009 [astro-ph.GA].

[13] P. C. Peters and J. Mathews, Gravitational radiation from point masses in a Keplerian orbit, Phys. Rev. **131**, 435 (1963).

[14] P. C. Peters, Gravitational Radiation and the Motion of Two Point Masses, Phys. Rev. **136**, B1224 (1964).

[15] I. Mandel and R. O'Shaughnessy, Compact Binary Coalescences in the Band of Ground-based Gravitational-Wave Detectors, Class. Quant. Grav. **27**, 114007 (2010), arXiv:0912.1074 [astro-ph.HE].

[16] C. L. Rodriguez and A. Loeb, Redshift Evolution of the Black Hole Merger Rate from Globular Clusters, Astrophys. J. Lett. **866**, L5 (2018), arXiv:1809.01152 [astro-ph.HE].

[17] G. Fragione and B. Kocsis, Black hole mergers from an evolving population of globular clusters, Phys. Rev. Lett. **121**, 161103 (2018), arXiv:1806.02351 [astro-ph.GA].

[18] M. Zevin, I. M. Romero-Shaw, K. Kremer, E. Thrane, and P. D. Lasky, Implications of Eccentric Observations on Binary Black Hole Formation Channels, Astrophys. J. Lett. **921**, L43 (2021), arXiv:2106.09042 [astro-ph.HE].

[19] Y. Kozai, Secular perturbations of asteroids with high inclination and eccentricity, Astron. J. **67**, 591 (1962).

[20] M. Lidov, The evolution of orbits of artificial satellites of planets under the action of gravitational perturbations of external bodies, Planetary and Space Science **9**, 719 (1962).

[21] J. Samsing, M. MacLeod, and E. Ramirez-Ruiz, The Formation of Eccentric Compact Binary Inspirals and the Role of Gravitational Wave Emission in Binary-Single Stellar Encounters, Astrophys. J. **784**, 71 (2014), arXiv:1308.2964 [astro-ph.HE].

[22] M. Zevin, J. Samsing, C. Rodriguez, C.-J. Haster, and E. Ramirez-Ruiz, Eccentric Black Hole Mergers in Dense Star Clusters: The Role of Binary–Binary Encounters, Astrophys. J. **871**, 91 (2019), arXiv:1810.00901 [astro-ph.HE].

[23] S. F. Portegies Zwart and S. McMillan, Black hole mergers in the universe, Astrophys. J. Lett. **528**, L17 (2000), arXiv:astro-ph/9910061.

[24] M. C. Miller and D. P. Hamilton, Production of intermediate-mass black holes in globular clusters, Mon. Not. Roy. Astron. Soc. **330**, 232 (2002), arXiv:astro-ph/0106188.

[25] I. M. Romero-Shaw, P. D. Lasky, and E. Thrane, Searching for Eccentricity: Signatures of Dynamical Formation in the First Gravitational-Wave Transient Catalogue of LIGO and Virgo, Mon. Not. Roy. Astron. Soc. **490**, 5210 (2019), arXiv:1909.05466 [astro-ph.HE].

[26] I. M. Romero-Shaw, P. D. Lasky, E. Thrane, and J. C. Bustillo, GW190521: orbital eccentricity and signatures of dynamical formation in a binary black hole merger signal, Astrophys. J. Lett. **903**, L5 (2020), arXiv:2009.04771 [astro-ph.HE].

[27] I. M. Romero-Shaw, P. D. Lasky, and E. Thrane, Signs of Eccentricity in Two Gravitational-wave Signals May Indicate a Subpopulation of Dynamically Assembled Binary Black Holes, Astrophys. J. Lett. **921**, L31 (2021), arXiv:2108.01284 [astro-ph.HE].

[28] I. M. Romero-Shaw, P. D. Lasky, and E. Thrane, Four Eccentric Mergers Increase the Evidence that LIGO–Virgo–KAGRA's Binary Black Holes Form Dynamically, Astrophys. J. **940**, 171 (2022), arXiv:2206.14695 [astro-ph.HE].

[29] R. Gamba, M. Breschi, G. Carullo, S. Albanesi, P. Rettegno, S. Bernuzzi, and A. Nagar, GW190521 as a dynamical capture of two nonspinning black holes, Nature Astron. **7**, 11 (2023), arXiv:2106.05575 [gr-qc].

[30] V. Gayathri, J. Healy, J. Lange, B. O'Brien, M. Szczepanczyk, I. Bartos, M. Campanelli, S. Klimenko, C. O. Lousto, and R. O'Shaughnessy, Eccentricity estimate for black hole mergers with numerical relativity simulations, Nature Astron. **6**, 344 (2022), arXiv:2009.05461 [astro-ph.HE].

[31] A. Bonino, R. Gamba, P. Schmidt, A. Nagar, G. Pratten, M. Breschi, P. Rettegno, and S. Bernuzzi, Inferring eccentricity evolution from observations of coalescing binary black holes, - (2022), arXiv:2207.10474 [gr-qc].

[32] H. L. Iglesias et al., Reassessing candidate eccentric binary black holes: Results with a model including higher-order modes, - (2022), arXiv:2208.01766 [gr-qc].

[33] T. A. Clarke, I. M. Romero-Shaw, P. D. Lasky, and E. Thrane, Gravitational-wave inference for eccentric binaries: the argument of periapsis, Mon. Not. Roy. Astron. Soc. **517**, 3778 (2022), arXiv:2206.14006 [gr-qc].

[34] A. M. Knee, I. M. Romero-Shaw, P. D. Lasky, J. McIver, and E. Thrane, A Rosetta Stone for Eccentric Gravitational Waveform Models, Astrophys. J. **936**, 172 (2022), arXiv:2207.14346 [gr-qc].

[35] A. Ramos-Buades, A. Buonanno, and J. Gair, Bayesian inference of binary black holes with inspiral-merger-ringdown waveforms using two eccentric parameters, Phys. Rev. D **108**, 124063 (2023), arXiv:2309.15528 [gr-qc].

[36] A. Buonanno and T. Damour, Effective one-body approach to general relativistic two-body dynamics, Phys. Rev. D **59**, 084006 (1999), arXiv:gr-qc/9811091.

[37] A. Buonanno and T. Damour, Transition from inspiral to plunge in binary black hole coalescences, Phys. Rev. D **62**, 064015 (2000), arXiv:gr-qc/0001013.

[38] T. Damour, B. R. Iyer, and A. Nagar, Improved resummation of post-Newtonian multipolar waveforms from circularized compact binaries, Phys. Rev. D **79**, 064004 (2009), arXiv:0811.2069 [gr-qc].

[39] Y. Pan, A. Buonanno, R. Fujita, E. Racine, and H. Tagoshi, Post-Newtonian factorized multipolar waveforms for spinning, non-precessing black-hole binaries, Phys. Rev. D **83**, 064003 (2011), [Erratum: Phys.Rev.D 87, 109901 (2013)], arXiv:1006.0431 [gr-qc].

[40] Y. Pan, A. Buonanno, A. Taracchini, L. E. Kidder, A. H. Mroué, H. P. Pfeiffer, M. A. Scheel, and B. Szilágyi, Inspiral-merger-ringdown waveforms of spinning, precessing black-hole binaries in the effective-one-body formalism, Phys. Rev. D **89**, 084006 (2014), arXiv:1307.6232 [gr-qc].

[41] A. Taracchini et al., Effective-one-body model for black-hole binaries with generic mass ratios and spins, Phys. Rev. D **89**, 061502 (2014), arXiv:1311.2544 [gr-qc].

[42] A. Bohé et al., Improved effective-one-body model of spinning, nonprecessing binary black holes for the era of gravitational-wave astrophysics with advanced detectors, Phys. Rev. D **95**, 044028 (2017), arXiv:1611.03703 [gr-qc].

[43] A. Nagar et al., Time-domain effective-one-body gravitational waveforms for coalescing compact binaries with nonprecessing spins, tides and self-spin effects, Phys. Rev. D **98**, 104052 (2018), arXiv:1806.01772 [gr-qc].

[44] R. Cotesta, A. Buonanno, A. Bohé, A. Taracchini, I. Hinder, and S. Ossokine, Enriching the Symphony of Gravitational Waves from Binary Black Holes by Tuning Higher Harmonics, Phys. Rev. D **98**, 084028 (2018), arXiv:1803.10701 [gr-qc].

[45] S. Babak, A. Taracchini, and A. Buonanno, Validating the effective-one-body model of spinning, precessing binary black holes against numerical relativity, Phys. Rev. D **95**, 024010 (2017), arXiv:1607.05661 [gr-qc].

[46] S. Ossokine et al., Multipolar Effective-One-Body Waveforms for Precessing Binary Black Holes: Construction and Validation, Phys. Rev. D **102**, 044055 (2020), arXiv:2004.09442 [gr-qc].

[47] A. Nagar and P. Rettegno, Efficient effective one body time-domain gravitational waveforms, Phys. Rev. D **99**, 021501 (2019), arXiv:1805.03891 [gr-qc].

[48] G. Riemenschneider, P. Rettegno, M. Breschi, A. Albertini, R. Gamba, S. Bernuzzi, and A. Nagar, Assessment of consistent next-to-quasicircular corrections and postadiabatic approximation in effective-one-body multipolar waveforms for binary black hole coalescences, Phys. Rev. D **104**, 104045 (2021), arXiv:2104.07533 [gr-qc].

[49] L. Pompili *et al.*, Laying the foundation of the effective-one-body waveform models SEOBNRv5: Improved accuracy and efficiency for spinning nonprecessing binary black holes, Phys. Rev. D **108**, 124035 (2023), arXiv:2303.18039 [gr-qc].

[50] D. Bini and T. Damour, Gravitational radiation reaction along general orbits in the effective one-body formalism, Phys. Rev. D **86**, 124012 (2012), arXiv:1210.2834 [gr-qc].

[51] T. Hinderer and S. Babak, Foundations of an effective-one-body model for coalescing binaries on eccentric orbits, Phys. Rev. D **96**, 104048 (2017), arXiv:1707.08426 [gr-qc].

[52] Z. Cao and W.-B. Han, Waveform model for an eccentric binary black hole based on the effective-one-body-numerical-relativity formalism, Phys. Rev. D **96**, 044028 (2017), arXiv:1708.00166 [gr-qc].

[53] X. Liu, Z. Cao, and L. Shao, Validating the Effective-One-Body Numerical-Relativity Waveform Models for Spin-aligned Binary Black Holes along Eccentric Orbits, Phys. Rev. D **101**, 044049 (2020), arXiv:1910.00784 [gr-qc].

[54] X. Liu, Z. Cao, and Z.-H. Zhu, A higher-multipole gravitational waveform model for an eccentric binary black holes based on the effective-one-body-numerical-relativity formalism, Class. Quant. Grav. **39**, 035009 (2022), arXiv:2102.08614 [gr-qc].

[55] X. Liu, Z. Cao, and L. Shao, Upgraded waveform model of eccentric binary black hole based on effective-one-body-numerical-relativity for spin-aligned binary black holes, Int. J. Mod. Phys. D **32**, 2350015 (2023), arXiv:2306.15277 [gr-qc].

[56] D. Chiaramello and A. Nagar, Faithful analytical effective-one-body waveform model for spin-aligned, moderately eccentric, coalescing black hole binaries, Phys. Rev. D **101**, 101501 (2020), arXiv:2001.11736 [gr-qc].

[57] A. Nagar, A. Bonino, and P. Rettegno, Effective one-body multipolar waveform model for spin-aligned, quasi-circular, eccentric, hyperbolic black hole binaries, Phys. Rev. D **103**, 104021 (2021), arXiv:2101.08624 [gr-qc].

[58] S. Albanesi, A. Nagar, and S. Bernuzzi, Effective one-body model for extreme-mass-ratio spinning binaries on eccentric equatorial orbits: Testing radiation reaction and waveform, Phys. Rev. D **104**, 024067 (2021), arXiv:2104.10559 [gr-qc].

[59] A. Placidi, S. Albanesi, A. Nagar, M. Orselli, S. Bernuzzi, and G. Grignani, Exploiting Newton-factorized, 2PN-accurate waveform multipoles in effective-one-body models for spin-aligned noncircularized binaries, Phys. Rev. D **105**, 104030 (2022), arXiv:2112.05448 [gr-qc].

[60] M. Khalil, A. Buonanno, J. Steinhoff, and J. Vines, Radiation-reaction force and multipolar waveforms for eccentric, spin-aligned binaries in the effective-one-body formalism, Phys. Rev. D **104**, 024046 (2021), arXiv:2104.11705 [gr-qc].

[61] A. Ramos-Buades, A. Buonanno, M. Khalil, and S. Ossokine, Effective-one-body multipolar waveforms for eccentric binary black holes with nonprecessing spins, Phys. Rev. D **105**, 044035 (2022), arXiv:2112.06952 [gr-qc].

[62] M. Boyle *et al.*, The SXS Collaboration catalog of binary black hole simulations, Class. Quant. Grav. **36**, 195006 (2019), arXiv:1904.04831 [gr-qc].

[63] The SXS binary black hole simulations catalog, `https://data.black-holes.org/waveforms`.

[64] A. Gamboa *et al.*, In preparation, .

[65] A. Nagar, G. Riemenschneider, G. Pratten, P. Rettegno, and F. Messina, Multipolar effective one body waveform model for spin-aligned black hole binaries, Phys. Rev. D **102**, 024077 (2020), arXiv:2001.09082 [gr-qc].

[66] A. Nagar and P. Rettegno, Next generation: Impact of high-order analytical information on effective one body waveform models for noncircularized, spin-aligned black hole binaries, Phys. Rev. D **104**, 104004 (2021), arXiv:2108.02043 [gr-qc].

[67] S. Albanesi, A. Nagar, S. Bernuzzi, A. Placidi, and M. Orselli, Assessment of effective-one-body radiation reactions for generic planar orbits, Phys. Rev. D **105**, 104031 (2022), arXiv:2202.10063 [gr-qc].

[68] S. Albanesi, A. Placidi, A. Nagar, M. Orselli, and S. Bernuzzi, New avenue for accurate analytical waveforms and fluxes for eccentric compact binaries, Phys. Rev. D **105**, L121503 (2022), arXiv:2203.16286 [gr-qc].

[69] A. Nagar and S. Albanesi, Toward a gravitational self-force-informed effective-one-body waveform model for nonprecessing, eccentric, large-mass-ratio inspirals, Phys. Rev. D **106**, 064049 (2022), arXiv:2207.14002 [gr-qc].

[70] S. Albanesi, S. Bernuzzi, T. Damour, A. Nagar, and A. Placidi, Faithful effective-one-body waveform of small-mass-ratio coalescing black hole binaries: The eccentric, nonspinning case, Phys. Rev. D **108**, 084037 (2023), arXiv:2305.19336 [gr-qc].

[71] A. Placidi, G. Grignani, T. Harmark, M. Orselli, S. Gliorio, and A. Nagar, 2.5PN accurate waveform information for generic-planar-orbit binaries in effective one-body models, Phys. Rev. D **108**, 024068 (2023), arXiv:2305.14440 [gr-qc].

[72] A. Nagar, R. Gamba, P. Rettegno, V. Fantini, and S. Bernuzzi, Effective-one-body waveform model for non-circularized, planar, coalescing black hole binaries: the importance of radiation reaction, (2024), arXiv:2404.05288 [gr-qc].

[73] A. Nagar, T. Damour, and A. Tartaglia, Binary black hole merger in the extreme mass ratio limit, Class. Quant. Grav. **24**, S109 (2007), arXiv:gr-qc/0612096.

[74] T. Damour and A. Nagar, Faithful effective-one-body waveforms of small-mass-ratio coalescing black-hole binaries, Phys. Rev. D **76**, 064028 (2007), arXiv:0705.2519 [gr-qc].

[75] E. Barausse, A. Buonanno, S. A. Hughes, G. Khanna, S. O'Sullivan, and Y. Pan, Modeling multipolar gravitational-wave emission from small mass-ratio mergers, Phys. Rev. D **85**, 024046 (2012), arXiv:1110.3081 [gr-qc].

[76] A. Taracchini, A. Buonanno, S. A. Hughes, and G. Khanna, Modeling the horizon-absorbed gravitational flux for equatorial-circular orbits in Kerr spacetime, Phys. Rev. D **88**, 044001 (2013), [Erratum: Phys.Rev.D 88, 109903 (2013)], arXiv:1305.2184 [gr-qc].

[77] A. Taracchini, A. Buonanno, G. Khanna, and S. A. Hughes, Small mass plunging into a Kerr black hole: Anatomy of the inspiral-merger-ringdown waveforms, Phys. Rev. D **90**, 084025 (2014), arXiv:1404.1819 [gr-qc].

[78] M. van de Meent, A. Buonanno, D. P. Mihaylov, S. Ossokine, L. Pompili, N. Warburton, A. Pound, B. Wardell, L. Durkan, and J. Miller, Enhancing the SEOBNRv5 effective-one-body waveform model with second-order gravitational self-force fluxes, Phys. Rev. D **108**, 124038 (2023), arXiv:2303.18026 [gr-qc].

[79] S. A. Teukolsky, Perturbations of a rotating black hole. 1. Fundamental equations for gravitational electromagnetic and neutrino field perturbations, Astrophys. J. **185**, 635 (1973).

[80] M. van de Meent and A. G. Shah, Metric perturbations produced by eccentric equatorial orbits around a Kerr black hole, Phys. Rev. D **92**, 064025 (2015), arXiv:1506.04755 [gr-qc].

[81] P. A. Sundararajan, G. Khanna, and S. A. Hughes, Towards adiabatic waveforms for inspiral into Kerr black holes. I. A New model of the source for the time domain perturbation equation, Phys. Rev. D **76**, 104005 (2007), arXiv:gr-qc/0703028.

[82] P. A. Sundararajan, G. Khanna, S. A. Hughes, and S. Drasco, Towards adiabatic waveforms for inspiral into Kerr black holes: II. Dynamical sources and generic orbits, Phys. Rev. D **78**, 024022 (2008), arXiv:0803.0317 [gr-qc].

[83] S. E. Field, S. Gottlieb, Z. J. Grant, L. F. Isherwood, and G. Khanna, A GPU-accelerated mixed-precision WENO method for extremal black hole and gravitational wave physics computations, Appl. Math. Comput. **5**, 97 (2023), arXiv:2010.04760 [math.NA].

[84] Y. Pan, A. Buonanno, L. T. Buchman, T. Chu, L. E. Kidder, H. P. Pfeiffer, and M. A. Scheel, Effective-one-body waveforms calibrated to numerical relativity simulations: coalescence of non-precessing, spinning, equal-mass black holes, Phys. Rev. D **81**, 084041 (2010), arXiv:0912.3466 [gr-qc].

[85] T. Damour and A. Nagar, Comparing Effective-One-Body gravitational waveforms to accurate numerical data, Phys. Rev. D **77**, 024043 (2008), arXiv:0711.2628 [gr-qc].

[86] G. Schott, On the motion of the Lorentz electron, The London, Edinburgh, and Dublin Philosophical Magazine and Journal of Science **29**, 49 (1915).

[87] S. Drasco and S. A. Hughes, Gravitational wave snapshots of generic extreme mass ratio inspirals, Phys. Rev. D **73**, 024027 (2006), [Erratum: Phys.Rev.D 88, 109905 (2013), Erratum: Phys.Rev.D 90, 109905 (2014)], arXiv:gr-qc/0509101.

[88] S. J. Kapadia, D. Kennefick, and K. Glampedakis, Do floating orbits in extreme mass ratio binary black holes exist?, Phys. Rev. D **87**, 044050 (2013), arXiv:1302.1016 [gr-qc].

[89] M. Colleoni, L. Barack, A. G. Shah, and M. van de Meent, Self-force as a cosmic censor in the Kerr overspinning problem, Phys. Rev. D **92**, 084044 (2015), arXiv:1508.04031 [gr-qc].

[90] L. Barack and O. Long, Self-force correction to the deflection angle in black-hole scattering: A scalar charge toy model, Phys. Rev. D **106**, 104031 (2022), arXiv:2209.03740 [gr-qc].

[91] Black Hole Perturbation Toolkit, (bhptoolkit.org).

[92] B. R. Iyer and C. M. Will, PostNewtonian gravitational radiation reaction for two-body systems, Phys. Rev. Lett. **70**, 113 (1993).

[93] B. R. Iyer and C. M. Will, PostNewtonian gravitational radiation reaction for two-body systems: Nonspinning bodies, Phys. Rev. D **52**, 6882 (1995).

[94] S. A. Hughes, The Evolution of circular, nonequatorial orbits of Kerr black holes due to gravitational wave emission, Phys. Rev. D **61**, 084004 (2000), [Erratum: Phys.Rev.D 63, 049902 (2001), Erratum: Phys.Rev.D 65, 069902 (2002), Erratum: Phys.Rev.D 67, 089901 (2003), Erratum: Phys.Rev.D 78, 109902 (2008), Erratum: Phys.Rev.D 90, 109904 (2014)], arXiv:gr-qc/9910091.